

Heavily Reddened Type 1 Quasars at $z > 2$ I: Evidence for Significant Obscured Black-Hole Growth at the Highest Quasar Luminosities

Manda Banerji^{1,2,3*}, S. Alaghband-Zadeh^{2,3}, Paul C. Hewett², Richard G. McMahon^{2,3}

¹*Department of Physics & Astronomy, University College London, Gower Street, London WC1E 6BT, UK.*

²*Institute of Astronomy, University of Cambridge, Madingley Road, Cambridge, CB3 0HA, UK.*

³*Kavli Institute for Cosmology, University of Cambridge, Madingley Road, Cambridge, CB3 0HA, UK.*

6 January 2015

ABSTRACT

We present a new population of $z > 2$ dust-reddened, Type 1 quasars with $0.5 \lesssim E(B - V) \lesssim 1.5$, selected using near infra-red (NIR) imaging data from the UKIDSS-LAS, ESO-VHS and *WISE* surveys. NIR spectra obtained using the Very Large Telescope (VLT) for 24 new objects bring our total sample of spectroscopically confirmed hyperluminous ($> 10^{13} L_{\odot}$), high-redshift dusty quasars to 38. There is no evidence for reddened quasars having significantly different $H\alpha$ equivalent widths relative to unobscured quasars. The average black-hole masses ($\sim 10^9$ – $10^{10} M_{\odot}$) and bolometric luminosities ($\sim 10^{47}$ erg/s) are comparable to the most luminous unobscured quasars at the same redshift, but with a tail extending to very high luminosities of $\sim 10^{48}$ erg/s. Sixty-six per cent of the reddened quasars are detected at $> 3\sigma$ at $22\mu\text{m}$ by *WISE*. The average $6\mu\text{m}$ rest-frame luminosity is $\log_{10}(L_{6\mu\text{m}}/\text{erg s}^{-1}) = 47.1 \pm 0.4$, making the objects among the mid-infrared brightest AGN currently known. The extinction-corrected space-density estimate now extends over three magnitudes ($-30 < M_i < -27$) and demonstrates that the reddened quasar luminosity function is significantly flatter than that of the unobscured quasar population at $z = 2 - 3$. At the brightest magnitudes, $M_i \lesssim -29$, the space density of our dust-reddened population exceeds that of unobscured quasars. A model where the probability that a quasar becomes dust-reddened increases at high luminosity is consistent with the observations and such a dependence could be explained by an increase in luminosity and extinction during AGN-fuelling phases. The properties of our obscured Type 1 quasars are distinct from the heavily obscured, Compton-thick AGN that have been identified at much fainter luminosities and we conclude that they likely correspond to a brief evolutionary phase in massive galaxy formation.

Key words: galaxies:active, (galaxies:) quasars: emission lines, (galaxies:) quasars: general, (galaxies:) quasars: individual

1 INTRODUCTION

Luminous dust-obscured quasars have been postulated to represent the missing evolutionary link between merger-induced starburst galaxies and ultraviolet (UV) bright quasars (Sanders et al. 1988) in theoretical models of galaxy formation (e.g. Hopkins et al. 2008; Narayanan et al. 2010). Samples of obscured active galactic nuclei (AGN) have been selected both in the hard X-ray (e.g. Brusa et al. 2010; Civano et al. 2012; LaMassa et al. 2013) and the mid-infrared (e.g. Stern et al. 2012; Assef et al. 2013; Donley et al.

2012). However, these surveys do not distinguish between a centrally concentrated obscuring medium, on parsec scales, close to the black-hole accretion disk (Urry & Padovani 1995; Antonucci 1993), and larger-scale obscuration due to gas and dust clouds in the quasar host galaxy (Martínez-Sansigre et al. 2005). Most hard X-ray and mid-infrared surveys (e.g. with the *Spitzer* Space Telescope) have covered relatively small areas of sky, probing obscured black-hole growth in relatively low-luminosity AGN, although the situation is now changing at mid infrared wavelengths with data from the *WISE* All-Sky Survey (Wright et al. 2010). In these faint samples, the number of obscured AGN is found to decrease with increasing luminosity. Constraints on obscured black-hole growth at the highest quasar luminosities however remain highly uncertain

* E-mail: m.banerji@ucl.ac.uk

and the relationship between hyperluminous ($> 10^{13} L_{\odot}$) obscured quasars and the now well-studied obscured AGN at low luminosities is also uncertain.

X-ray surveys also show a curious lack of high Eddington ratio ($L/L_{\text{Edd}} > 0.1$) objects with N_{H} between 3×10^{21} and $3 \times 10^{22} \text{ cm}^{-2}$ (Fabian 2012; Raimundo et al. 2010). Objects with such properties, i.e. high luminosity combined with a significant gas/dust column, could possess massive AGN-driven outflows. The apparent upper limit to the distribution of Eddington ratios could be a selection bias, as most X-ray surveys do not cover a large enough area to detect the rarest and brightest quasars with high Eddington ratios. Such objects have traditionally been selected through their rest-frame UV emission which is very sensitive to dust extinction and therefore biased against detecting luminous quasars with even moderate gas column densities. The Sloan Digital Sky Survey (SDSS) Data Release (DR) 7 quasar sample (Schneider et al. 2010) now mitigates the situation to a degree. The flux limit in the redder i -band allows some intrinsically very luminous objects with $E(B - V) \simeq 0.5$ to be included (Richards et al. 2003). The new SDSS-III BOSS DR10 quasar survey (Pâris et al. 2014) reaches fainter optical magnitudes than the SDSS and has significantly increased the number of quasars known at the main epoch of galaxy formation at $z \sim 2 - 3$. Populations of red quasars are detected in the BOSS data (Ross et al. 2014) including the first large sample of narrow-line Type 2 obscured quasars at high redshifts (Alexandrov et al. 2013), some of which also show evidence for broad-lines in the near infrared (Greene et al. 2014). However, even with the fainter flux-limit, BOSS cannot find quasars with $E(B - V) \gtrsim 0.6$.

Wide-field infrared surveys now cover much of the observable sky, providing the sensitivity to detect dusty, intrinsically luminous, broad-line quasars. The 2MASS survey has identified optically obscured quasars that are also radio-loud (e.g. Glikman et al. 2007; Urrutia et al. 2009; Glikman et al. 2012); the radio selection using FIRST data is necessary to eliminate contaminant populations but means that the majority of AGN are excluded by the selection. In radio-loud red quasars (e.g. Webster et al. 1995), the red colours can arise as a result of the presence of a red synchrotron component (Francis et al. 2001; Whiting et al. 2001) rather than due to dust. The flux-limit of the 2MASS survey has also meant that these red quasars are predominantly at low-redshift although with some of the most luminous quasars seen out to $z > 2$ (Glikman et al. 2012). A concern at low-redshifts is that host galaxy contamination can redden the observed colours of these quasars. The galaxy spectral energy distribution (SED) peaks at $\sim 1 \mu\text{m}$, corresponding to the inflection point in the AGN SED. This feature is in the NIR JHK filters at $z \sim 0.2 - 1$. However, at $z \sim 0.7$, the FIRST-2MASS red quasars are seen to be associated with merging galaxy hosts (Urrutia et al. 2008), consistent with an interpretation where the objects are in a transition phase from starburst to unobscured quasar. Extending these investigations to focus on the main epoch of galaxy and black-hole formation at $z \sim 2 - 3$ will be instructive in understanding the importance of this obscured phase in galaxy formation.

The *WISE* All-Sky Survey operating at mid-infrared wavelengths, has recently led to the identification of a new population of hyperluminous dust-obscured galaxies (HyLIRGs), whose spectral energy distributions (SEDs) are consistent with a dominant contribution from AGN (Eisenhardt et al. 2012; Wu et al. 2012). These HyLIRGs are also postulated to represent the evolutionary link between massive starbursts and luminous quasars. The *WISE* samples are complementary to near infrared selected samples as they enable

the selection of much more highly obscured AGN. The AGN that have so far been identified by *WISE* are seen to be Compton thick (Stern et al. 2014). Broad emission lines originating from gas close to the black-hole are therefore completely concealed and estimating virial black-hole masses is no longer possible.

The wide-field NIR UKIDSS Large Area Survey (LAS) (Lawrence et al. 2007) and VISTA Hemisphere Survey (VHS; McMahon et al. 2013) allow us to probe much fainter than was possible using 2MASS and enable selection of complementary samples of obscured quasars to the *WISE* survey. In a survey over $> 1000 \text{ deg}^2$ of the UKIDSS and VHS data we were able to identify a population of $z \sim 2 - 3$, $E(B - V) \sim 0.8$ quasars (Banerji et al. 2012, 2013 - hereafter B12 and B13 respectively), demonstrating that contaminant populations can be eliminated without having to rely on radio pre-selection. Our new quasars are among the most bolometrically luminous quasars known ($L_{\text{bol}} > 10^{47} \text{ erg/s}$) but, as a result of their significant dust-extinctions, are often invisible in wide-field optical surveys like SDSS. The sample represents a population of hyperluminous quasars at $z \sim 2 - 3$ whose extinction properties are intermediate between UV-selected, essentially unobscured, quasars and the very heavily obscured AGN emerging from *WISE*. Similar obscured luminous quasars showing strong evidence for corresponding to the AGN feedback phase, are also now emerging from multi-wavelength degree-scale galaxy surveys such as COSMOS (Brusa et al. 2010; Bongiorno et al. 2014; Brusa et al. 2014). Indeed the brightest obscured quasar selected from the COSMOS survey is the faintest obscured quasar selected in our wide-field UKIDSS search for similar objects (B12). The ability to isolate the luminous AGN population with intermediate levels of extinction means that it is now possible to investigate objects with extinctions corresponding to reddenings of $0 \lesssim E(B - V) \lesssim 3$. New insight into the importance of non-spherical geometries (i.e. ‘unified schemes’) and evolution, involving specific phases during AGN lifetimes, for explaining the distribution of extinction properties can be expected.

Our survey also led to the identification of the prototype quasar: ULASJ1234+0907, the reddest broad-line quasar currently known. With an Eddington ratio of 0.65 (B12) and a neutral hydrogen column-density of $9 \times 10^{21} \text{ cm}^{-2}$ (Banerji et al. 2014), ULASJ1234+0907 lies in the sparsely-populated high L/L_{Edd} and intermediate gas column regime found from the statistics of hard X-ray sources. Among the most luminous quasars known at both X-ray and far-infrared wavelengths, ULASJ1234+0907 may represent the emerging phase of a supermassive black-hole shortly after a starburst (Banerji et al. 2014). Larger surveys for NIR-selected, dust-obscured, luminous quasars may unearth more objects like ULASJ1234+0907.

The current paper presents a much larger survey for heavily dust-reddened, hyperluminous broad-line quasars at $z = 2 - 3$, where the abundance of gas-rich, star-forming galaxies provides a natural explanation for the presence of extended obscuring media in these luminous quasars. Combined with objects presented in B12 and B13, the new sample allows us to characterise in detail the demographics of the luminous reddened quasar population at $z \sim 2.5$, including the direct calculation of the space density over a three-magnitude interval. We emphasise that the parameter space sampled by our survey is very different from that of X-ray surveys for obscured AGN in deep fields covering only a few square degrees. A companion paper (Alaghband-Zadeh et al., in preparation) investigates the spatially resolved properties of the new reddened quasars from the IFU data presented here.

The structure of the paper is as follows. First, the observational

data, including the photometric selection (Section 2) and spectroscopic follow-up (Section 3), is described. The generation of the key physical properties of the quasars, including extinction estimates, luminosities and black-hole masses, is covered in Section 4, prior to consideration of the object properties derived from WISE photometric data in Section 5. The primary scientific result, the calculation of the population space density and luminosity function is presented in Section 6, followed by a summary of the main results in Section 7. Throughout the paper we assume a flat Λ CDM cosmology with $h_0=0.70$, $\Omega_m = 0.30$ and $\Omega_\Lambda=0.70$. The VHS magnitudes are on the AB system where the conversions from Vega to AB used are: $J = +0.937$, $H = +1.384$, $K = 1.839$. All WISE magnitudes and colours are on the Vega system.

2 PHOTOMETRIC SELECTION

2.1 Colour Selection of Reddened Quasars

We make use of new wide-field infrared photometry over ~ 1500 deg^2 from VHS and WISE, in order to identify luminous reddened quasar candidates in the southern hemisphere. In addition, we also use >3000 deg^2 of imaging data from the UKIDSS Large Area Survey (LAS) (Lawrence et al. 2007) in the northern hemisphere, to select a sample of the reddest quasars, such as ULASJ1234+0907 (Banerji et al. 2014). The details of the colour selection has been presented in B13 but we provide a summary here. Candidates must be morphologically classified as point sources in the K -band (i.e. with $kclass = -1$; González-Solares et al. 2011) and possess extremely red NIR colours of $(J - K)_{AB} > 1.6$. The morphology cut is necessary to ensure that we isolate a population of quasars at high redshifts corresponding to the peak epoch of black-hole accretion activity, where the host galaxy light in the NIR is sub-dominant. The red colours of these quasars in the NIR, can then be attributed to dust-reddening rather than galaxy starlight. A WISE colour-cut of $(W1 - W2) > 0.85$ is then applied to separate quasars from stars. Candidates are required to be detected at a signal-to-noise ratio (S/N) of >5 in both the WISE $W1$ and $W2$ bands. As shown in B13, this selection is extremely effective in isolating rare populations of heavily reddened quasars at high redshifts.

Our quasar sample encompasses several different survey regions. Below we describe the candidate selection criteria used in each of these regions as well as ancillary multi-wavelength data that were used to prioritise targets for spectroscopy. After applying the colour and morphology selections in each of our survey areas, all candidates were visually inspected in order to remove spurious sources. The most common such spurious sources are instances of close neighbours in the VHS data with separations of <3 arcsec and where the WISE photometry appears to be blended, making the WISE colours unreliable. The survey regions, selection criteria and number of candidates are summarised in Table 1.

- *The VHS-DES Stripe82 Region:* This region ($20\text{h} < \text{RA} < 0\text{h}$, $-2^\circ < \text{DEC} < 2^\circ$) overlaps the SDSS Stripe82 multi-epoch survey where the coadded data reaches $\simeq 2$ mag fainter than the main SDSS survey (Annis et al. 2011). As discussed in B12, we used the deep coadd SDSS Stripe82 photometry to select only the subset of red $(J - K)$ candidates that are also faint and red at optical wavelengths. Candidates were therefore required to satisfy the additional selection criteria: $i_{AB} > 20.5$ and $(i - K)_{AB} > 2.5$.

Many of our infrared-selected candidates that failed this cut and are blue and bright in the optical, possess SDSS or BOSS spectra. Later, in Section 2.2, we show the SDSS spectra to demon-

strate which object populations are eliminated by the optical cuts and to determine what the contaminants may be in regions where we do not yet have optical coverage. Our selection produced 10 candidates down to a flux limit of $K_{AB} < 18.8$ over 129 deg^2 , after visual inspection to remove spurious and blended sources. Two of the 10, ULASJ2150–0055 and ULASJ2224–0015, were observed as part of the sample described in B12. One more candidate (SDSSJ211805.27+010344.7) has an optical spectrum from SDSS where it is classified as a $z \sim 5$ quasar, although with low confidence. The optical spectrum does not show any obvious emission lines. The remaining seven sources were added to our spectroscopic target list.

- *The VHS-DES SPT Region:* In this region ($20\text{h} < \text{RA} < 0\text{h}$, $-60^\circ < \text{DEC} < -45^\circ$) we identify a total of 29 candidates down to a flux limit of $K_{AB} < 18.8$ over 498 deg^2 . In addition, over the 83 deg^2 area of the ‘SPT Deep Field’ (centred at $23\text{h} < \text{RA} < 00\text{h}$ and $-60^\circ < \text{DEC} < -50^\circ$), the selection was extended to $K_{AB} < 19.3$, giving four additional candidates. The SPT Deep Field benefits from multi-wavelength coverage from *Spitzer* (Ashby et al. 2013), *Herschel* and *XMM-Newton*, which can be used to investigate the multi-wavelength properties of our quasars.

- *The VHS-ATLAS SGC Region:* In this region covered by VHS ($20\text{h} < \text{RA} < 0\text{h}$, $-20^\circ < \text{DEC} < -2^\circ$) we only selected candidates over the $\sim 488 \text{ deg}^2$ area with optical photometry from the SDSS. The VHS-ATLAS regions have shallower J -band coverage compared to VHS-DES (McMahon et al. 2013) and the selection of candidates with extremely red $(J - K)$ colours is prone to contamination from larger numbers of spurious sources. However, unlike the VHS-DES region, VHS-ATLAS also benefits from Y -band coverage, which we used to impose an additional selection criterion: $Y > J$. Three candidates were selected and verified to be faint and red at optical wavelengths based on the SDSS data.

- *The VHS-ATLAS NGC Region:* This region ($13\text{h}40 < \text{RA} < 16\text{h}20$ and $-20^\circ < \text{DEC} < -2^\circ$) encompasses the area used for target selection in our pilot survey (B13). Nine bright targets with $K_{AB} < 18.4$ were selected from 421 deg^2 . Two of which, VHSJ1350-0503 and VHSJ1409-0830, were observed in B13. The remaining seven candidates were added to our spectroscopic target list.

- *The UKIDSS-LAS Data Release 10 $(H - K) > 1.4$ Sample:* Finally, using the UKIDSS-LAS DR10, covering a total area of 3131 deg^2 at $\text{DEC} < 20^\circ$ (observable from the Very Large Telescope), we also constructed a candidate list of the reddest quasars which satisfy the additional colour selection criterion of $(H - K) > 1.4$ and have $K < 18.9$. These would correspond to the dustiest hyperluminous quasars at these high redshifts with $E(B - V) \gtrsim 1.2$ and the objective was to find more quasars like ULASJ1234+0907 (Banerji et al. 2014). Three of these extremely red candidates were visible at the time of observations and were also added to our spectroscopic target list.

Our final candidate list comprised a total of 53 spectroscopic targets, excluding candidates already observed by B12 and B13. As described below, 48 of these targets were successfully observed, with 24 classified as broad-line quasars. The candidate list includes a complete sample of 41 objects, with $K_{AB} < 18.9$, over a region of 1115 deg^2 , selected to provide quantitative constraints on the space density of the reddened quasar population.

Table 1. Summary of survey regions and selection criteria for reddened quasars presented in this work plus B12 and B13. Several survey regions are spectroscopically incomplete. Column 4 gives the number of candidates observed, with the total number of candidates and the percentage completeness in brackets. Column 5 gives the corresponding information for the number of candidates yielding spectroscopic redshifts, with the total number of spectroscopic targets and the percentage redshift yield in brackets.

Survey Region	Selection Criterion	Area/deg ²	Nobs (Ncand)	Nw/z (Nobs)
$K < 18.4$ Bright Sample				
VHS-DES SPT ^a	$(J - K) > 1.6, (W1 - W2) > 0.85$	498	12(12,100%)	7(12,58%)
VHS-ATLAS NGC ^{a,c}	$(J - K) > 1.6, (W1 - W2) > 0.85, Y > J$	421	5(9,56%)	3(5,60%)
VHS-ATLAS SGC ^a	$(J - K) > 1.6, (W1 - W2) > 0.85, Y > J$	488	1(1,100%)	0(1,0%)
VHS-DES S82-W ^{a,b}	$(J - K) > 1.6, (W1 - W2) > 0.85$	129	5(5,100%)	1(5,20%)
$i > 20.5, (i - K) > 2.5$				
UKIDSS-LAS S82-E ^b	$(J - K) > 1.6, (W1 - W2) > 0.85$	116	5(7,71%)	5(5,100%)
$i > 20.5, (i - K) > 2.5$				
UKIDSS-LAS DR10 ^{a,b}	$(J - K) > 1.6, (W1 - W2) > 0.85, (H - K) > 1.4$	3131	6(5,83%)	3(5,60%)
$18.4 < K < 18.9$ Intermediate Sample				
VHS-DES SPT ^a	$(J - K) > 1.6, (W1 - W2) > 0.85$	498	17(17,100%)	9(17,53%)
VHS-DES S82-W ^{a,b}	$(J - K) > 1.6, (W1 - W2) > 0.85$	129	4(4,100%)	2(4,50%)
$i > 20.5, (i - K) > 2.5$				
VHS-ATLAS SGC ^a	$(J - K) > 1.6, (W1 - W2) > 0.85, Y > J$	488	2(2,100%)	2(2,100%)
$18.9 < K < 19.3$ Faint Sample				
VHS-DES SPT Deep ^a	$(J - K) > 1.6, (W1 - W2) > 0.85$	83	4(4,100%)	1(4,25%)

^aThis Work ^bBanerji et al. 2012 ^cBanerji et al. 2013

2.2 Optically Bright Reddened Quasar Candidates with SDSS Spectroscopy

Before describing our NIR spectroscopic observations, we examine the SDSS/BOSS optical spectra for the optically-bright objects in the VHS-DES Stripe82. There are five reddened quasar candidates, based on their $(J - K)$ and $(W1 - W2)$ colours, which have $i < 20.5$ and/or $(i - K) < 2.5$ and were therefore removed from our final candidate list. Spectra for these sources are shown in Fig. 1. Three objects are at $z < 0.6$; two appear to be morphologically compact star-forming galaxies while one is a low-redshift quasar.

The two remaining optically bright candidates with SDSS spectra are both quasars at higher redshifts. ULASJ2219+0036 (SDSS J221930.42+003626.3), a quasar at $z = 1.196$, was also identified in B12, where NIR spectroscopy was presented. No emission lines were detected, confirming that our NIR spectroscopy can fail to identify reddened quasars at low redshifts. SDSS J220325.00-004002.8, a quasar at $z = 2.565$, possesses a spectrum with a blue UV continuum and is therefore not a heavily dust-reddened quasar. We note that both these high redshift quasars have spectroscopy from the BOSS survey but not from the SDSS Data Release 7.

As demonstrated in Ross et al. (2014), red quasars selected from the SDSS/BOSS surveys constitute a heterogeneous population including reddened Type 1 quasars, Type 2 quasars, Broad Absorption Line quasars, as well as sources with extreme emission line equivalent widths. Each of these populations is interesting in its own right but in this work, we are specifically interested in investigating the properties of the reddened Type 1 quasars and our target selection is designed to isolate this subset of red objects.

3 SPECTROSCOPIC FOLLOW-UP

Follow-up of our reddened quasar spectroscopic targets was conducted in Visitor Mode over three full nights in 2013 July using the SINFONI spectrograph on the Very Large Telescope (VLT). The seeing ranged from 0.5 to 1.0 arcsec with a median of 0.78 arcsec.

The quasar candidates were expected to cover a broad range in redshift, similar to the samples in B12 & B13, and use of the SINFONI $H + K$ filters was therefore requested. However, due to technical difficulties, only the SINFONI R=4000 K -band grating was available. The K -filter has a wavelength range of 1.9–2.5 μm , corresponding to a redshift range of $2.1 < z < 2.7$ for $H\alpha$ and redshifts $3.1 < z < 4.1$ for $H\beta$ and $[\text{OIII}]\lambda\lambda 4959, 5007$. At redshifts $0.5 < z < 2.1$ however, no strong emission lines are visible in the K -band so this represents a *redshift desert* for our survey. ULASJ2219+0036 (see Section 2.2) is an example of a candidate in the redshift desert.

The dispersion is 2.5 Å per pixel. Observations were carried out in noAO mode, utilising the largest field of view of the instrument, which is 8×8 arcsec. The targets were offset by ± 1.5 arcsec in RA and DEC from the centre of the IFU for sky-subtraction purposes. Apart from the choice of filter, the observational setup is identical to that in B12. The total integration time was adjusted depending on the K -band magnitude of each source and the prevailing conditions at the time of observation. Fainter targets therefore have much longer exposure times, chosen such that any broad-lines present should be detected at high S/N in the binned spectra.

All data were reduced using standard ESO pipeline recipes using the *gasgano* data reduction package. Data reduction steps included dark subtraction, non-linearity corrections, flat-fielding, sky subtraction, extraction and wavelength calibration. Relative flux calibration was performed using telluric standards observed at similar airmass to the target. Typically, four to five telluric standards were observed through the night. Due to the absence of spectrophotometric standards in the NIR, absolute flux calibration was achieved by normalising the spectra using the K -band magnitudes of the targets.

From our final list of 53 spectroscopic targets, 48 objects were successfully observed with SINFONI over the three nights. Twenty-four show broad-lines in the NIR K -band spectrum and are therefore spectroscopically confirmed to be quasars, with redshifts assigned assuming that the emission line is $H\alpha$. We note that the observed equivalent widths of these lines are inconsistent with corresponding to other Balmer lines (e.g. $\text{Pa}\alpha$, $\text{Pa}\beta$) at lower redshifts,

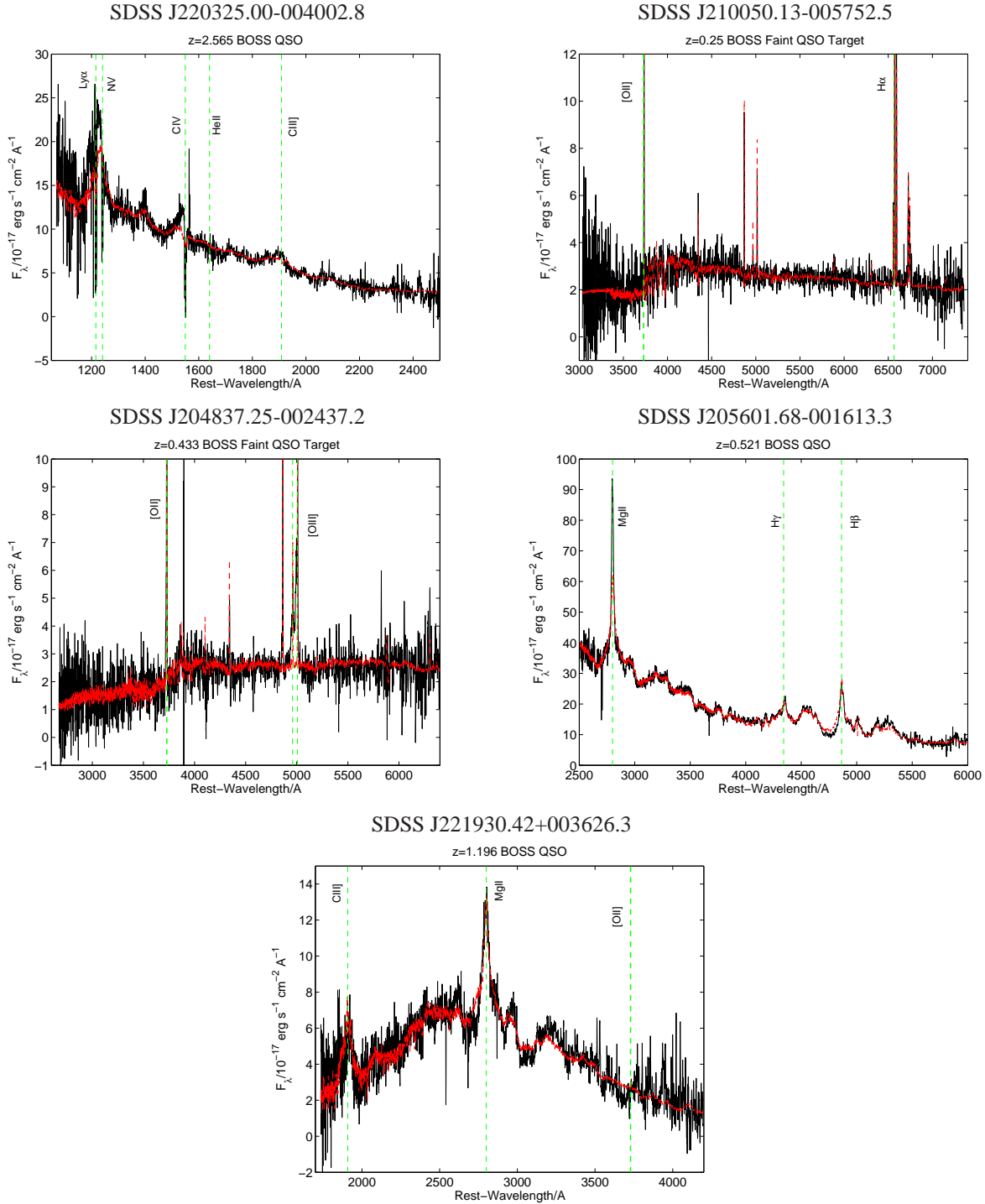


Figure 1. SDSS spectra of optically bright reddened quasar candidates (black solid) along with the best model-fit used for the redshift determinations (dashed red). Note, all of these were quasar targets within BOSS.

which are expected to be at least an order of magnitude weaker (Glikman et al. 2006). The spectroscopically confirmed quasars together with their coordinates, K -band magnitudes, redshifts and exposure times are listed in Table 2. One dimensional spectra, extracted over regions maximising the S/N of the $H\alpha$ emission line, are presented for all objects in Fig. A1.

4 DEMOGRAPHICS OF THE REDDENED QUASAR POPULATION

4.1 Spectral Energy Distributions, Dust Extinctions & Bolometric Luminosities

To provide estimates of dust extinctions and luminosities we fit the multi-wavelength photometric data for our confirmed reddened

Table 2. Summary of Spectroscopically Confirmed Reddened Quasars.

Name	RA	DEC	K_{AB}	Redshift	Exposure time (s)
VHS-DES SPT Region					
VHSJ2024-5623	306.1074	-56.3898	18.76	2.282	1800
VHSJ2028-4631	307.0083	-46.5325	18.87	2.464	1800
VHSJ2028-5740	307.2092	-57.6681	17.25	2.121	800
VHSJ2048-4644	312.0435	-46.7387	18.78	2.182	1600
VHSJ2100-5820	315.1403	-58.3354	18.47	2.360	1600
VHSJ2101-5943	315.3311	-59.7291	16.68	2.313	320
VHSJ2115-5913	318.8818	-59.2188	17.63	2.115	800
VHSJ2130-4930	322.7490	-49.5032	18.47	2.448	1600
VHSJ2141-4816	325.3530	-48.2830	18.54	2.655	1600
VHSJ2212-4624	333.0796	-46.4101	18.72	2.141	1800
VHSJ2220-5618	335.1398	-56.3107	16.72	2.220	320
VHSJ2227-5203	336.9491	-52.0582	18.80	2.656	2200
VHSJ2235-5750	338.9331	-57.8372	17.95	2.246	1000
VHSJ2256-4800	344.1444	-48.0088	17.80	2.250	1000
VHSJ2257-4700	344.2589	-47.0157	18.51	2.156	1600
VHSJ2306-5447	346.5011	-54.7881	18.17	2.372	1000
VHSJ2332-5240	353.0387	-52.6780	19.16	2.450	2400
VHS-ATLAS SGC and NGC Regions					
VHSJ1556-0835	239.1571	-8.5952	18.20	2.188	1200
VHSJ2143-0643	325.8926	-6.7206	18.48	2.383	1600
VHSJ2144-0523	326.2394	-5.3881	18.71	2.152	1600
VHS-DES Stripe82 Region					
VHSJ2109-0026	317.3630	-0.4497	18.59	2.344	1600
VHSJ2355-0011	358.9394	-0.1893	18.42	2.531	1600
UKIDSS-LAS DR10 ($H - K$) > 1.4					
ULASJ0123+1525	20.8022	+15.4230	18.59	2.629	1200
ULASJ2315+0143	348.9843	+1.7307	18.38	2.560	400

quasars using the quasar SED models of Maddox et al. (2008, 2012). In the VHS-DES SPT region the data consists of photometry in *JHK* and *WISE W1* and *W2*. For the Stripe82, VHS-ATLAS and UKIDSS regions, optical photometry (from the Stripe82 coadd survey and SDSS) is also available and has been utilised in the SED fitting. The fitting procedure is described in B12 and accounts for the effect of the observed $H\alpha$ equivalent width on the $(J - K)$ colours as follows. The equivalent width of the $H\alpha$ emission line in our base SED model has been derived by fitting to the observed colours (*ugrizYJHK*) of luminous, unobscured, quasars in SDSS DR7 that possess SDSS and UKIDSS photometry. The quasar SED model (Maddox et al. 2012) takes into account luminosity-dependent changes in the $H\alpha$ equivalent width due to the Baldwin effect (Baldwin 1977). The base quasar-SED model has already been shown to provide a very good match to the observed colours of luminous SDSS DR7 quasars over the redshift range $0.2 < z < 4.0$ (Maddox et al. 2012). The default rest-frame equivalent width of the $H\alpha$ line in our $z=2.3$ model is $\simeq 250 \text{ \AA}$.

For each of our reddened quasars, we estimate the rest-frame $H\alpha$ equivalent widths directly from the spectra. All equivalent widths are calculated by integrating the line within $\pm 3\sigma$, where σ is derived from a single Gaussian fit to the line profile. The continuum is defined beyond this 3σ region out to $\pm 10000 \text{ km/s}$ from the $H\alpha$ line centroid. The exact details of the equivalent width calculations are not important as measurements are made consistently for both the SED model and the observed spectra. The rest-frame $H\alpha$ equivalent widths for each of our reddened quasars are given in Table A1 and the median value is $\simeq 270 \text{ \AA}$, which is consistent with the value for the unobscured quasar population. There is therefore no evidence that the reddened quasars have unusual $H\alpha$ equivalent widths relative to their unobscured counterparts.

There are, however, a few examples of reddened quasars with $H\alpha$ equivalent widths of up to $\simeq 500 \text{ \AA}$. For comparison, the K -band filter in the VISTA survey has an effective width of 3090 \AA or 940 \AA in the rest-frame at $z=2.3$. When deriving $E(B - V)$ -estimates, it is important that we account for the effect of the $H\alpha$ line on the continuum K -band flux. We therefore proceed as follows. The $H\alpha$ line in the SED model is scaled to have the same rest-frame equivalent width present in each individual reddened quasar. As is evident from Table A1 the scaling-factor is close to unity for the majority of quasars. The $E(B - V)$ values are then derived by fitting the scaled SED to all the observed photometry available for each quasar. In this way, the specific contribution to the K -band flux by the $H\alpha$ emission line in each quasar is taken into account and the $E(B - V)$ estimates are independent of the emission-line strength.

Our model also includes a luminosity dependent contribution from a host galaxy. Even allowing for the effects of extinction on the quasar SED, at the redshifts and K -band magnitudes of our sample, the NIR-colours of the majority of the objects are dominated by the quasar SED. Recall that a key element in the sample selection is that the candidates must be unresolved in the K -band and, by selection, the host-galaxy contribution cannot be large. The form of the host-galaxy SED and exact contribution to the observed NIR-colours are thus not significant in the context of reproducing the *JHKW1W2* photometry.

The strongest constraints on the reddening for each quasar predominantly come from the $J - K$ colour, which probes rest-frame wavelengths of $\sim 3400\text{--}6400 \text{ \AA}$, below the inflexion in the quasar SEDs at $\simeq 10000 \text{ \AA}$ and above the UV-portion of the spectrum where different extinction curves exhibit quite different forms. The derived values of $E(B - V)$ are thus completely insensitive to

which extinction curve (e.g. curves appropriate for the Milky Way, Large or Small Magellanic Clouds) is incorporated in the model fits. Given the photometric uncertainties, the estimates of $E(B-V)$ are accurate to $\simeq \pm 0.1$ mag. Extinction values are summarised in Table 3 and the median $E(B-V)$ is found to be 0.8 mag, consistent with the values reported in B12 and B13.

As demonstrated in Banerji et al. (2014), these dust extinction estimates derived from SED-fitting to the broadband photometry, are in excellent agreement with those from independent X-ray observations, even for the reddest and therefore dustiest quasars. The observed quasar SEDs are de-reddened using the $E(B-V)$ values, assuming an SMC-like extinction law (Pei 1992), and the optical luminosity at rest-frame 5100Å is calculated¹. The observed and de-reddened i -band quasar magnitudes, together with the de-reddened i -band absolute magnitudes and bolometric luminosities are presented in Table 3. Note, these i -band absolute magnitudes are related to the SDSS $M_{i[z=2]}$ magnitudes via $M_i = M_{i[z=2]} + 0.596$. The total luminosities are estimated using a bolometric correction factor of 7 applied to the rest-frame 5100Å luminosity (Netzer et al. 2007)².

4.2 Black-Hole Masses

Single-epoch quasar black-hole masses are normally derived based on a virial estimator, employing the widths of broad emission lines and assuming a calibration between the size of the broad-line region and the quasar luminosity. The calibration has been derived using reverberation mapping techniques at low redshift (Kaspi et al. 2000, 2005) and for relatively low-luminosity AGN; the validity of extrapolating the trends to high redshift and higher luminosities, still remains uncertain. In addition, virial black-hole mass estimates can be sensitive to the choice of broad line used, and the details of the line-fitting. A further complication can result if there are significant inflows and outflows affecting the gas close to the accreting black-hole that can artificially broaden the observed linewidths. If reddened quasars do correspond to the AGN-feedback phase in galaxy formation, such inflows and outflows would be more predominant in our sample and indeed several of the H α line profiles shown in Figure A2 clearly show evidence for very broad wings that could result from such flows.

Despite these caveats, single-epoch black-hole masses are still widely used and there is general consistency between mass estimates obtained from different broad-lines (Shen et al. 2011; Matsuoka et al. 2013). We therefore provide such mass estimates for our reddened quasar sample. Specifically, we employ the mass estimator of Vestergaard & Peterson (2006), using the calibration between H α and H β linewidths from Greene & Ho (2005):

$$\text{FWHM}_{\text{H}\beta} = (1.07 \pm 0.07) \times 10^3 \left(\frac{\text{FWHM}_{\text{H}\alpha}}{10^3 \text{ km s}^{-1}} \right)^{1.03 \pm 0.03} \text{ km s}^{-1} \quad (1)$$

$$M_{\text{BH}}/M_{\odot} = 10^{6.91} \left(\frac{\text{FWHM}_{\text{H}\beta}}{1000 \text{ km s}^{-1}} \right)^2 \left(\frac{L_{5100}}{10^{44} \text{ erg s}^{-1}} \right)^{0.5} \quad (2)$$

¹ As with the determination of the $E(B-V)$ -values, the derived optical luminosities are insensitive to which conventional extinction curve is employed.

² A bolometric correction factor of closer to 9 has also been used in the literature (Shen et al. 2011) and would increase our estimated bolometric luminosities by ~ 0.1 dex.

where L_{5100} is estimated using the best-fit model SEDs of each quasar. The H α rest-frame full-width-half-maximum (FWHM) is calculated from either a single- or a double-Gaussian fit to the line profile in the velocity range $\pm 10000 \text{ km s}^{-1}$. Double Gaussians are only used if they produce a statistically significant improvement to the line-profile fit corresponding to a lower mean-fit error. All Gaussian components are constrained to possess FWHM in the range $1000\text{--}10\,000 \text{ km s}^{-1}$, ensuring they trace broad-line region gas. Errors on the black-hole masses are derived by propagating the mean fit error on the FWHM measurements. Contributions to the H α emission-line profile from any narrow component present are small and we verified that including such a narrow Gaussian component did not alter significantly the FWHM of the broad single- or double-Gaussian components. Parametrization of any narrow H α components, which could potentially be tracing star formation in the quasar host galaxy, is discussed in Alaghband-Zadeh et al (in preparation).

The Gaussian line fits are included in Figure A2, while the FWHM values and derived black-hole masses are tabulated in Table A1 and Table 3 respectively.

4.3 Comparison to Unobscured Quasars from SDSS

The black-hole masses and bolometric luminosities can be used to derive Eddington ratios (L/L_{Edd}) which are typically > 0.1 , as was found in B12 and B13. The reddened quasars therefore appear to be massive black holes, accreting at a high rate, resulting in their very high luminosities. Large numbers of unobscured, luminous and highly accreting black-holes are known, e.g. from SDSS (Schneider et al. 2007) and BOSS (Pâris et al. 2014), and the luminosity function and space density of the obscured and unobscured populations are of potential interest. We define a sample of 2081 ‘unobscured’ quasars from SDSS DR7, with redshifts $2.1 < z < 2.7$ and magnitudes $K < 18.9$ as well as black-hole mass and bolometric luminosity estimates from Shen et al. (2011). The combined sample of spectroscopically confirmed reddened quasars from B12, B13 and this paper, over the same redshift range and brighter than $K < 18.9$ represents the ‘reddened’-quasar population. The distribution of black-hole masses and luminosities for the two samples are shown in Fig. 2. The mean black-hole masses and bolometric luminosities are $\log_{10}(M_{\text{BH}}/M_{\odot}) = 9.7 \pm 0.4$, $\log_{10}(L_{\text{bol}}/\text{erg s}^{-1}) = 47.1 \pm 0.4$ and $\log_{10}(M_{\text{BH}}/M_{\odot}) = 9.3 \pm 1.1$, $\log_{10}(L_{\text{bol}}/\text{erg s}^{-1}) = 47.0 \pm 0.2$ for the reddened and unobscured samples respectively.

The distributions of black-hole mass and luminosity overlap significantly (Fig. 2), but there is an indication that the reddened quasars possess a tail out to higher bolometric luminosities and black-hole masses. Several selection effects and systematic errors could be responsible for this observed tail. The black hole masses, derived from UV-emission lines for objects in SDSS and H α for the reddened population, may not be on exactly the same scale. Progress is being made via direct comparison of emission-line properties in quasar samples (Matsuoka et al. 2013; Tilton & Shull 2013) but the uncertainty in black hole mass estimates from individual emission lines remains significant (e.g. Shen et al. 2011). More importantly, inflows and outflows are likely to be more common in the reddened population, thought to be caught in the AGN radiative feedback phase. The presence of such flows could add significant additional spread to the observed linewidths, increasing black-hole masses by factors of a few (B12). The black-hole masses should therefore be interpreted with caution.

The bolometric luminosities of the samples may also differ

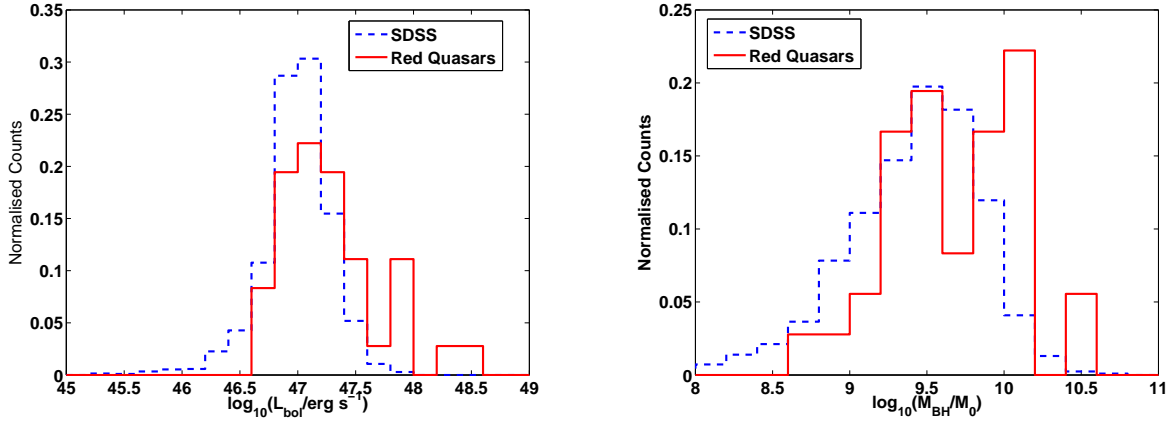


Figure 2. Distribution of bolometric luminosity (left) and black-hole mass (right) for the red and unobscured quasar populations (see descriptions in Section 4.3). There is significant overlap between the samples in both luminosity and mass, although there is a suggestion that the red population includes a tail of quasars with very high bolometric luminosities and black-hole masses.

systematically. Luminosities for the unobscured quasar sample are calculated using the 1350\AA rest-frame luminosity and assume a different model quasar SED to ours. Most likely, however, is a selection against the most luminous quasars in the SDSS resulting from the bright i -band flux-limit of 15.0 mag (c.f. the values for the reddened quasars in Col. 4 of Table 3).

Overall, notwithstanding the caveats summarised above, we can conclude that the reddened quasar sample consists of a population of very high mass black-holes, comparable to the most massive black-holes included in the SDSS quasar sample.

5 INFRARED SEDS FROM WISE

Comparing the multi-wavelength properties of the reddened quasar sample to other well-studied galaxy and AGN populations at similar redshifts helps in understanding the origin of the sample. The availability of the *WISE* photometry, probing rest-frame wavelengths out to $\gtrsim 3\text{ }\mu\text{m}$ for objects detected in the *W3*-band, provides information for a key portion of quasar SEDs. An unobscured comparison sample is defined by selecting 1604 SDSS DR7 and DR10 quasars with $2.1 < z < 2.7$, $K_{AB} < 18.9$ and detections in the *WISE* *W123*-bands - hereafter the ‘SDSS sample’.

The reddened quasar sample was selected using a $(W1 - W2) > 0.85$ colour cut as detailed in Section 2 and are therefore, by definition, red in the bluer *WISE* bands³. We show the *WISE* colours of our spectroscopically confirmed quasars in Fig. 3 on the colour-colour locus introduced by Wright et al. (2010). All the objects are detected at $> 3\sigma$ in the *W3* $12\text{ }\mu\text{m}$ band and the majority have *W1W2W3*-colours placing them in the QSO/Seyfert locus of

Wright et al. (2010). Just a few of the reddest sources extend into the Obscured AGN locus.

Fig. 3 suggests that, crudely, the reddened quasars are indistinguishable from unobscured quasars in terms of their *WISE* colours. We can test this quantitatively by fitting a power-law to the observed *WISE* fluxes in the *W1*, *W2* and *W3* bands of the form $\lambda F_\lambda \propto \lambda^{\beta_{\text{NIR}}}$. Emission from hot dust is expected to dominate the SEDs over the $1\text{--}4\text{ }\mu\text{m}$ rest-frame wavelength range probed by the *WISE* passbands. We find a mean value of $\beta_{\text{NIR}}=0.69$ in our sample⁴ with a standard deviation of 0.29. The mean NIR power-law index for the SDSS sample is 0.50 ± 0.26 , consistent with the results from Wang et al. (2013) and Hao et al. (2011).

The SDSS and reddened-quasar power-law indices agree within 1σ of the population deviation and the steeper mean value for the reddened quasars is consistent with the most obscured of our quasars showing some extinction at rest-frame wavelengths of $1\text{--}2\text{ }\mu\text{m}$, which steepens the slope of the SED. Fig. 4 shows the distribution of β for both populations. The high β_{NIR} tail is due to the reddest quasars in our sample, with $E(B - V) \gtrsim 0.8$, as expected.

Several recent studies have focused on the subset of high redshift AGN that are extremely bright in the *W4* $22\text{ }\mu\text{m}$ band. Ross et al. (2014) studied a sample of SDSS and BOSS spectroscopically confirmed quasars with $W4 \leq 8$ mag and the *WISE* consortium have selected hyperluminous infrared galaxies, with $W4 \lesssim 7.7$ mag, that are extremely red in their $(W1 - W2)$ colours (Eisenhardt et al. 2012; Wu et al. 2012). Our selection for reddened quasars does not use the $22\text{ }\mu\text{m}$ fluxes, although, by selecting objects that are bright in the *K*-band, we are by definition not sensitive to the *WISE* ‘*W12*’ drop-outs. Twenty-five of our 38 reddened quasars are detected at $> 3\sigma$ in the *W4* band. Of these, 14 have $W4 \leq 8$ mag and 11 have $W4 \leq 7.7$ mag, 37 and 29 per cent of the sample respectively. The $22\text{ }\mu\text{m}$ -detected objects are generally the most bolometrically luminous quasars in our sample, as expected.

For objects detected in the *WISE* *W4*-band, rest-frame luminosities at $6\text{ }\mu\text{m}$ can be estimated using the *W3* and *W4*

³ All *WISE* photometry presented in this section are taken from the new, improved *WISE* data reductions available through the *AllWISE* data release. However, the *WISE* main survey catalogue was used for the target selection as the *AllWISE* reductions were not available at the time. We find that the *WISE* and *AllWISE* fluxes are generally consistent apart from a single quasar: VHSJ2024-5623. The quasar satisfied the $(W1 - W2) > 0.85$ colour cut in the original *WISE* data release with $W1 = 16.52$ and $W2 = 15.49$ but has revised magnitudes in *AllWISE* of $W1 = 16.17$ and $W2 = 15.44$.

⁴ The convention for β_{NIR} employed here is in wavelength rather than frequency space compared to our previous work (B13). The two slopes are related by $\beta_{\text{NIR}} = \beta_{\text{NIR}}(\text{B13}) + 1$.

Table 3. Best-fit dust extinction, reddened and de-reddened optical i -band magnitudes, absolute i -band magnitudes, bolometric luminosities, black-hole masses and Eddington ratios of the reddened quasars.

Name	E(B-V)	i_{AB}^{red}	i_{AB}^{dered}	M_i	$\log_{10}(L_{\text{bol}}/\text{erg s}^{-1})$	$\log_{10}(M_{\text{BH}}/M_{\odot})$	IEdd	$\text{dm/dt } (M_{\odot}\text{yr}^{-1})$
VHS-DES SPT Region								
VHSJ2024-5623	0.6	22.9	17.8	-27.37	46.7	9.8 ± 0.1	0.06	9
VHSJ2028-4631	0.6	22.9	17.9	-27.49	46.7	9.2 ± 0.2	0.2	9
VHSJ2028-5740	1.2	24.3	14.6	-30.18	47.9	10.1 ± 0.1	0.4	127
VHSJ2048-4644	0.7	23.2	17.4	-27.65	46.8	9.2 ± 0.1	0.3	11
VHSJ2100-5820	0.8	23.6	16.5	-28.49	47.1	9.1 ± 0.1	0.8	24
VHSJ2101-5943	0.8	21.8	14.9	-30.03	47.8	10.5 ± 0.1	0.1	106
VHSJ2115-5913	1.0	23.5	15.4	-29.48	47.5	9.3 ± 0.1	1.4	61
VHSJ2130-4930	0.9	24.7	16.5	-28.75	47.2	9.5 ± 0.2	0.4	31
VHSJ2141-4816	0.8	23.8	16.1	-29.10	47.3	9.6 ± 0.2	0.4	40
VHSJ2212-4624	0.8	23.7	17.2	-27.64	46.9	9.9 ± 0.1	0.07	14
VHSJ2220-5618	0.8	21.6	14.9	-30.09	47.8	9.9 ± 0.1	0.5	106
VHSJ2227-5203	0.9	25.0	16.3	-29.15	47.4	10.0 ± 0.1	0.2	41
VHSJ2235-5750	0.6	21.9	16.9	-28.28	47.1	10.1 ± 0.1	0.07	20
VHSJ2256-4800	0.6	21.7	16.7	-28.49	47.1	10.1 ± 0.1	0.08	24
VHSJ2257-4700	0.7	23.0	17.3	-27.67	46.9	9.5 ± 0.1	0.2	13
VHSJ2306-5447	0.7	23.2	17.1	-28.15	47.0	10.0 ± 0.1	0.08	18
VHSJ2332-5240	0.6	23.4	18.0	-27.39	46.7	9.5 ± 0.1	0.1	8
VHS-ATL SGC and NGC Regions								
VHSJ1556-0835	0.7	22.7	16.9	-28.15	47.0	8.6 ± 0.1	1.9	19
VHSJ2143-0643	0.8	23.8	16.7	-28.33	47.1	10.0 ± 0.1	0.09	22
VHSJ2144-0523	0.6	22.6	17.7	-27.33	46.7	9.9 ± 0.1	0.04	9
VHS-DES Stripe82 Region								
VHSJ2109-0026	0.7	23.3	17.2	-27.95	46.9	9.8 ± 0.1	0.1	15
VHSJ2355-0011	0.7	23.2	16.6	-28.67	47.2	10.1 ± 0.1	0.09	27
UKIDSS-LAS DR10 ($H - K$) > 1.4								
ULASJ0123+1525	1.3	27.7	15.4	-30.12	47.8	9.7 ± 0.2	0.9	114
ULASJ2315+0143	1.1	26.2	16.1	-29.43	47.5	10.1 ± 0.2	0.2	57

Table 4. *WISE* $W3$ and $W4$ magnitudes for all reddened quasars detected at $> 3\sigma$ at $22\mu\text{m}$ along with the rest-frame $6\mu\text{m}$ luminosity.

Name	$W3$ (mags)	$W4$ (mags)	$\log_{10}(L_{6\mu\text{m}}/\text{erg s}^{-1})$
ULASJ0123+1525	8.69 ± 0.03	6.33 ± 0.06	47.8
ULASJ0144-0114	10.07 ± 0.05	8.02 ± 0.21	47.1
ULASJ0221-0019	10.46 ± 0.06	8.11 ± 0.17	46.9
ULASJ1234+0907	9.17 ± 0.04	7.28 ± 0.17	47.4
VHSJ1350-0503	10.62 ± 0.07	8.59 ± 0.26	46.7
VHSJ1409-0830	10.33 ± 0.06	8.31 ± 0.23	46.9
ULASJ1455+1230	10.43 ± 0.05	8.11 ± 0.15	46.3
ULASJ1539+0557	9.10 ± 0.03	6.56 ± 0.06	47.8
VHSJ2028-5740	9.15 ± 0.03	7.01 ± 0.08	47.3
VHSJ2048-4644	10.42 ± 0.08	7.92 ± 0.18	46.9
VHSJ2100-5820	10.70 ± 0.10	8.14 ± 0.24	46.9
VHSJ2101-5943	9.25 ± 0.03	6.84 ± 0.07	47.4
VHSJ2115-5913	9.48 ± 0.04	7.06 ± 0.08	47.2
VHSJ2130-4930	10.69 ± 0.09	8.52 ± 0.33	46.9
VHSJ2141-4816	10.46 ± 0.07	7.68 ± 0.16	47.3
ULASJ2200+0056	10.23 ± 0.06	7.80 ± 0.17	47.2
VHSJ2212-4624	11.02 ± 0.12	8.37 ± 0.27	46.7
VHSJ2220-5618	8.77 ± 0.03	6.37 ± 0.05	47.6
VHSJ2227-5203	10.11 ± 0.06	8.02 ± 0.22	47.2
VHSJ2235-5750	9.97 ± 0.05	7.84 ± 0.17	47.0
VHSJ2256-4800	9.67 ± 0.04	7.52 ± 0.13	47.1
VHSJ2257-4700	10.77 ± 0.09	8.43 ± 0.28	46.7
ULASJ2315+0143	9.57 ± 0.04	7.03 ± 0.10	47.5
VHSJ2332-5240	11.51 ± 0.20	8.45 ± 0.31	46.9
VHSJ2355-0011	9.83 ± 0.05	7.40 ± 0.14	47.3

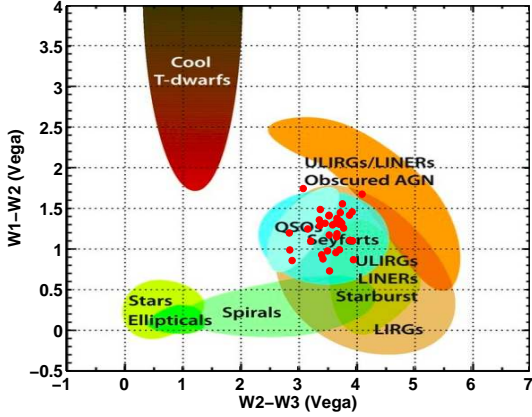


Figure 3. Location of reddened quasars in *WISE* colour-colour plane taken from Wright et al. (2010) showing that they overlap the QSO/Seyfert locus.

photometry. At the median redshift of $z = 2.3$ for our sample, the $W3$ band corresponds to $3.6\mu\text{m}$ and the $W4$ band corresponds to $6.7\mu\text{m}$. The $6\mu\text{m}$ luminosities are calculated via linear interpolation, using the rest-frame wavelengths corresponding to the $W3$ and $W4$ magnitudes, and the results are given in Table 4 and illustrated in Fig. 5. The average rest-frame $6\mu\text{m}$ luminosity is $\log_{10}(L_{6\mu\text{m}}/\text{erg s}^{-1}) = 47.1 \pm 0.4$. For a comparable SDSS DR7+DR10 sample of 1336 $2.1 < z < 2.7$ quasars with $K < 18.9$ and $> 3\sigma$ detections in the $W4$ band, the average luminosity is $\log_{10}(L_{6\mu\text{m}}/\text{erg s}^{-1}) = 46.8 \pm 0.2$. There are six SDSS quasars with $\log_{10}(L_{6\mu\text{m}}/\text{erg s}^{-1}) > 47.5$ (four from SDSS DR7 and two from SDSS DR10). The brightest of these six is the well-known gravitationally-lensed Cloverleaf quasar (Magain et al. 1988). SDSSJ000610.67+121501.2 ($z = 2.309$) and SDSSJ155102.79+084401.1 ($z = 2.520$), the two DR10 objects, were presented in the extremely red sample studies by Ross et al. (2014). By comparison, our reddened quasar sample, selected using imaging data covering less than a third of the total SDSS imaging area ($\sim 14,555 \text{ deg}^2$ from Pâris et al. 2014), includes four quasars with $\log_{10}(L_{6\mu\text{m}}/\text{erg s}^{-1}) > 47.5$, highlighting the increased prevalence of such luminous quasars among the obscured sample. Compared to *WISE*-selected HyLIRGs where the most luminous object at $6\mu\text{m}$, WISEJ1814+3412 (Eisenhardt et al. 2012), has $\log_{10}(L_{6\mu\text{m}}/\text{erg s}^{-1}) = 47.30 \pm 0.05$ (Stern et al. 2014), the reddened quasar sample is also extreme, with seven objects more luminous than WISEJ1814+3412.

Finally, we compare the $6\mu\text{m}$ luminosities to the bolometric luminosities in Table 3, and find a typical bolometric correction factor of ~ 2 , consistent with a model in which a large fraction of the total luminosity is re-radiated at mid infrared wavelengths. This bolometric correction from the mid infrared is also broadly consistent with that derived for the most luminous essentially unobscured quasars in SDSS and *WISE* (Weedman et al. 2012). As the $6\mu\text{m}$ rest-frame luminosities are inferred directly from the observed photometry without any assumptions regarding the dust extinction law and the form of the quasar SED, this analysis corroborates our conclusion in Section 4.1, that our reddened quasars correspond to some of the most intrinsically luminous quasars known.

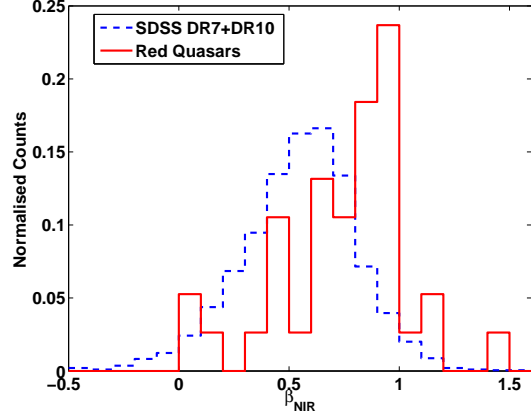


Figure 4. Distribution of NIR power-law indices, β_{NIR} , fit in the rest-frame wavelength range $1-4\mu\text{m}$ both for our reddened quasar sample and SDSS unobscured quasars over the same redshift range and down to the same K -band flux limit.

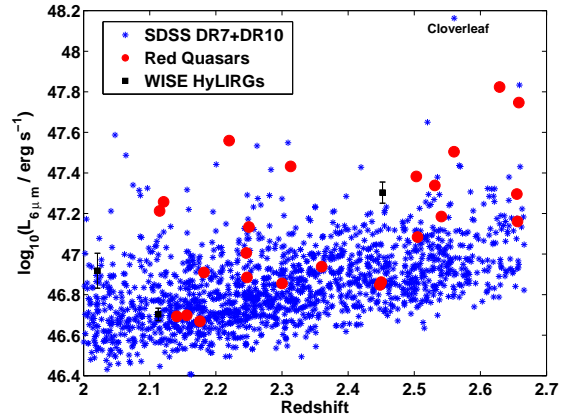


Figure 5. Redshift versus rest-frame $6\mu\text{m}$ luminosity for our reddened quasars compared to unobscured quasars from SDSS as well as 3 *WISE* HyLIRGs from Stern et al. (2014). The brightest unobscured quasar on this plot is the lensed Cloverleaf quasar.

6 OBSCURED BLACK-HOLE GROWTH AT THE HIGHEST QUASAR LUMINOSITIES

With a sample of 38 reddened quasars ($E(B - V) \geq 0.5$), of which 36 lie at $z > 2$, now in place, a direct comparison of their space density to that of unobscured quasars can be made. As deep X-ray and mid-infrared surveys have focussed on studying much fainter, dusty, AGN, the sample allows us to address the key question of how many very luminous quasars are dust-obscured at redshifts $z \sim 2 - 3$. We begin by considering the selection function and completeness of our reddened quasar sample.

6.1 Sample Completeness

6.1.1 Morphology Cut

The sample selection (Section 2) includes a requirement that candidates are unresolved in the K -band. While eliminating contamination by low-redshift quasars, where host galaxies can contribute

significantly to the observed colours (B12), it is necessary to quantify the fraction of high-redshift quasars that may also be excluded. To assess such incompleteness, we select a sample of unobscured quasars from the SDSS DR7 (Schneider et al. 2010) and SDSS DR10 (Pâris et al. 2014) quasar catalogues, with redshifts $2.1 < z < 2.7$ and magnitudes $K < 19.3$. There are a total of 7871 quasars that satisfy these criteria. The cumulative fraction of unobscured quasars classified as unresolved as a function of K -band magnitude is shown in Fig. 7. At the bright-end ($K < 18$), almost 90 per cent of the quasars are unresolved, with the fraction decreasing to just under 70 per cent at the faint limit. Only four of the 48 reddened quasar candidates are in the faintest magnitude bin and, using the distribution of candidate K -magnitudes, we calculate the incompleteness due to the image morphology constraint to be 20-25 per cent.

6.1.2 $(J - K)$ Colour Cut

The NIR colour-cut of $(J - K) > 1.6$ is designed to isolate the most highly reddened Type 1 broad-line quasars. Fig. 6 shows model quasar $(J - K)$ colours, calculated using our quasar SED model (Section 4.1), over the redshift range of our sample, as a function of the extinction parameter $E(B - V)$. Some dependence of $(J - K)$ colour on redshift is present; higher redshift quasars have bluer $(J - K)$ colours due to the $H\alpha$ emission line moving out of the K -band. However, there is a tight correspondence between extinction and colour, with the $(J - K) > 1.6$ threshold predicted to define a quasar sample with $E(B - V) \gtrsim 0.5$.

A potential concern is that quasars with very large $H\alpha$ equivalent widths and somewhat lower $E(B - V)$ values form a significant fraction of the sample. The direct measurements of the $H\alpha$ equivalent widths for the reddened quasars (Table A1), however, demonstrate that the presence of such objects is not a factor. The highest equivalent width quasar in our sample has an equivalent width of only a factor of ~ 2 larger than the average equivalent width in unobscured quasars of similar luminosity. The average $H\alpha$ equivalent widths however are very similar to those seen in unobscured quasars, confirming that the reddened quasars we have selected do not have unusual equivalent widths relative to the unreddened population.

The systematic dependence of the threshold $E(B - V)$ as a function of redshift to satisfy the $(J - K) > 1.6$ selection, evident in Fig. 6, is directly taken into account when estimating the space-density (Section 6.3). The S/N of the K -band photometry used in the sample selection is high and any apparent increase in the observed number of objects due to Eddington bias (Eddington 1913) is small. The S/N of the J -band photometry is somewhat lower and the $E(B - V)$ selection at a given redshift, resulting from the $(J - K) > 1.6$ colour cut, is thus blurred, with some objects lost from the sample and others included due to photometric errors. This could be a concern if the $E(B - V)$ distribution was changing significantly at the boundary of our selection box ($E(B - V) \sim 0.5$), in which case unequal numbers of objects may be scattered out of the sample relative to the numbers of objects that are scattered in. However, estimates of the form of the $E(B - V)$ distribution from SDSS (Hopkins et al. 2004) and near-IR selected samples (Maddox et al. 2012) strongly suggest that the $E(B - V)$ distribution is not changing significantly and our sample should thus represent an accurate estimate of number of objects with $E(B - V)$ exceeding the limits calculated.

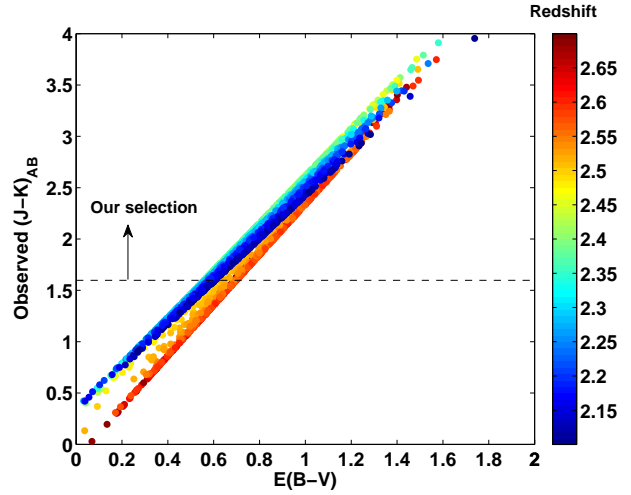


Figure 6. Observed, reddened $(J - K)$ colour as a function of extinction $E(B - V)$ for a set of simulated quasars assuming the base SED model described in Section 4.1 and an SMC-like extinction law. Points are colour-coded by the redshift of the quasar. The dashed horizontal line shows our colour selection for the reddened quasars.

6.1.3 WISE Colour Cut

We employ the same SDSS sample of unobscured quasars used in Section 6.1.1 to determine the incompleteness of the reddened quasar sample due to the application of the restriction that $WISE (W1 - W2) \geq 0.85$. The $WISE$ colours of the reddened quasar sample are themselves affected by the presence of dust. Specifically, at the median redshift of the sample ($z = 2.3$), the $W1$ and $W2$ magnitudes of a quasar possessing an $E(B - V)$ of 0.5 mag are 0.75 and 0.53 mag fainter respectively. The requirement that $(W1 - W2) \geq 0.85$ for reddened quasars with $E(B - V) \gtrsim 0.5$ therefore corresponds to $(W1 - W2) \geq 0.63$ for the unobscured SDSS sample.

Figure 7 also shows the cumulative fraction of the unobscured SDSS sample with $(W1 - W2) \geq 0.63$, $W1_{S/N} > 5$ and $W2_{S/N} > 5$ (dot-dashed line). This fraction is > 90 per cent for most of the magnitude range but falls to $\simeq 85$ per cent in the faintest magnitude bin, used in the 83 deg^2 VHS-DES SPT Deep Field survey.

The cumulative fraction of quasars, with redshifts $2.1 < z < 2.7$, that satisfy both the $(J - K)$ and $(W1 - W2)$ colour cuts, plus the unresolved morphology constraint, i.e. the combined sample photometric completeness, is also shown in Fig. 7. More than 70 per cent of quasars satisfy all our selection criteria at $K = 18.9$ with the completeness falling to just under 65 per cent at $K = 19.3$.

6.2 Redshift Completeness

In addition to the candidate photometric completeness, the effectiveness of the spectroscopic observations for determining redshifts and hence reliable object classifications must be considered. Fig. A1 shows that the high equivalent-width, broad, $H\alpha$ emission lines are clearly detected at high S/N, even at the faint K -band limit (e.g. VHSJ2332-5240) or when the line is at the edge of the wavelength interval (e.g. VHSJ2227-5203). All $H\alpha$ lines have $S/N > 4$. The observational strategy (Section 3), where integration times (Table 2) were adjusted to achieve a minimum S/N for each target

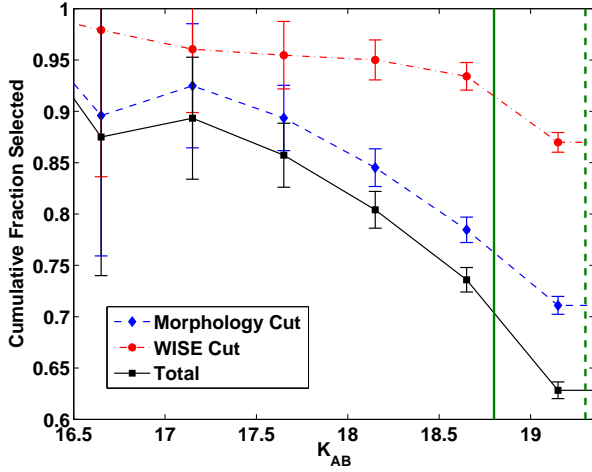


Figure 7. Cumulative fraction of SDSS DR7 and DR10 quasars at $2.1 < z < 2.7$ and $K < 19.3$, that are also classified as point sources in the K -band, as a function of K -band magnitude (dashed line). The dot-dashed line shows the cumulative fraction of SDSS quasars that have $(W1 - W2) > 0.63$ (corresponding to $(W1 - W2) > 0.85$ for $E(B - V) > 0.5$). The solid line shows the cumulative fraction of SDSS high redshift quasars that satisfy both the morphology and *WISE* colour selection. The solid vertical line marks the magnitude limit used for the majority of our reddened quasar sample while the dashed vertical line shows the magnitude limit used in the 83 sq-deg VHS-DES SPT deep field. We can see that >70 per cent of true high redshift quasars would satisfy all our selection criteria at $K=18.9$ and this completeness falls to just under 65 per cent at $K = 19.3$.

sufficient to allow detection of broad emission lines, thereby ensures that the redshift completeness is close to 100 per cent within the redshift interval $2.1 < z < 2.7$. Fig. 8 shows the rest-frame equivalent width of the $H\alpha$ line as a function of the quasar K -band magnitude. No significant correlation between the two quantities is present and, particularly for the faintest quasars, a range of equivalent widths is evident. There is no evidence to suggest that, for the faintest sources, our survey is preferentially detecting quasars with large $H\alpha$ equivalent widths.

In the space-density analysis that follows, we first consider a ‘Bright Sample’, from the VHS-DES SPT, VHS-DES S82-W and VHS-ATLAS SGC regions, as summarised in Table 1. These three regions cover a total area of 1115 deg^2 and all 29 candidates with $K_{AB} < 18.9$ possess spectra. Twenty one of the 29 candidates have redshifts. In addition, We also consider a ‘Faint Sample’, based on the $K_{AB} < 19.3$ sample, covering the 83 deg^2 SPT Deep Field, where, again, all candidates possess spectra.

6.3 The Reddened Quasar Space Density

We calculate the V/V_{max} weighted (Schmidt 1968; Avni & Bahcall 1980) estimate of the reddened quasar space density from the 21 reddened quasars in the Bright Sample. Using the best-fit SED for each reddened quasar, we can calculate its absolute magnitude as well as the redshift range and therefore total volume V , within which it would have satisfied our survey selection criteria. Our space density calculations assume the quasar SED model from Section 4.1 in order to derive k -corrections and therefore absolute magnitudes and bolometric luminosities. As our SED model is slightly different from the one used in

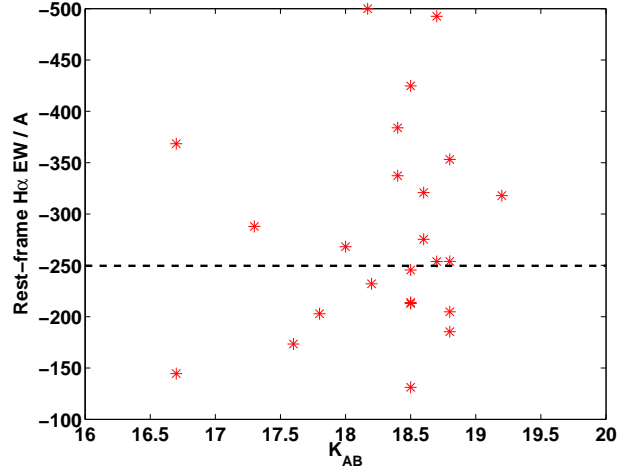


Figure 8. Rest-frame equivalent width of the $H\alpha$ line in our reddened quasars as a function of the K -band magnitude. The horizontal dashed line represents the average $H\alpha$ equivalent widths of unobscured quasars at the same redshift and luminosity. The $H\alpha$ lines have a range of equivalent widths between $\sim 0.5 - 2$ times the equivalent widths in unobscured quasars. Particularly at the faint-end of the sample, a range of $H\alpha$ equivalent widths is evident with no strong correlation between the K -band magnitude and the equivalent width.

SDSS (Ross et al. 2013) and in order to allow comparison with investigations by other groups, we provide a table with the i -band and K -band k -correction from our model in Table B1. However, we note that differences in k -corrections derived from our template and that of Ross et al. (2013) are expected to be small given that both templates are able to reproduce the observed colours of SDSS quasars (Maddox et al. 2012; Ross et al. 2013). The maximum available survey volume, V_{max} is the co-moving volume within $2.1 < z < 2.7$. The cumulative volume and completeness-corrected number density in each absolute magnitude bin is then given by:

$$N(M < M_i)_{\text{corr}}/\text{Mpc}^3 = \frac{f_{\text{sky}}}{V_{\text{max}}} \sum_{j=1}^{N_{\text{bin}}} \frac{1}{c(K) \times V_j/V_{\text{max}}} \quad (3)$$

The error on these cumulative number counts is:

$$\sigma_{N(M < M_i)} = \frac{f_{\text{sky}}}{V_{\text{max}}} \sum_{j=1}^{N_{\text{bin}}} \frac{1}{(c(K) \times V_j/V_{\text{max}})^2} \quad (4)$$

where f_{sky} denotes the fraction of area on the sky encompassed by our survey and $c(K)$ is the K -band magnitude dependent photometric completeness of each quasar calculated using the completeness curve in Fig. 7. The resulting cumulative space density is shown in Fig. 9 together with the equivalent space density for unobscured quasars derived from the SDSS+BOSS luminosity function (LF; Ross et al. 2013) over exactly the same redshift and absolute magnitude range as the reddened sample. As our luminosity function for reddened quasars extends to brighter absolute magnitudes than the SDSS+BOSS quasars, we assume the parametric double power-law form of the unobscured quasar luminosity function and integrate this parametric luminosity function over the appropriate redshift and luminosity ranges to compare to the reddened quasars in Fig. 9. We consider two best-fit forms for this parametric luminosity function for unobscured quasars from Ross et al.

(2013). Firstly, a luminosity and density evolution (LEDE) model and secondly a pure luminosity evolution model (PLE). We note that the SDSS+BOSS luminosity function is constrained in the redshift range $2.2 < z < 3.5$ and only a very modest extrapolation of the luminosity function and redshift-evolution is necessary to compare with our new data. In Ross et al. (2013), a pure luminosity evolution (PLE) model has instead been fit to the data at $z < 2.2$ but the effect on the cumulative LEDE model based number counts of the unobscured quasars plotted in Fig. 9 is small. We also note that the systematic differences in k-corrections between our models and those used by BOSS, are expected to be smaller than the bin size in Fig. 9.

We find that the LF of the reddened quasars is significantly flatter than that of the SDSS+BOSS quasars over the entire magnitude range. At bright absolute magnitudes ($M_i < -29$), the reddened quasars possess larger space densities than predicted by the SDSS+BOSS LEDE LF, but the more steeply rising SDSS+BOSS quasar LF means the unobscured quasars become significantly more common at magnitudes $M_i > -27.5$. The much flatter increase in the number of quasars as a function of decreasing luminosity leads to very different interpretations regarding the fraction of the total energy liberated by the Type 1 AGN population in an ‘obscured’ phase, compared to previous investigations which probed only the most luminous quasars (e.g. White et al. 2003; Glikman et al. 2007). Our survey now covers enough dynamic range in luminosity to demonstrate that while the numbers of obscured ($0.5 \lesssim E(B - V) \lesssim 1.5$) quasars are significant at the highest luminosities, their space density shows a much shallower rise relative to unobscured quasars at these redshifts. There is no evidence from our data that the reddened quasars have significantly different $H\alpha$ equivalent width distributions relative to unobscured quasars so we are unlikely to be missing a population of very low equivalent width objects but with similar levels of reddening as in our sample. As such, these reddened broad-line quasars are likely to be sub-dominant relative to the unobscured quasars in terms of their contribution to the total energy liberated during the luminous quasar phase. For reference, our $K = 18.9$ magnitude limit corresponds to $M_i \sim -27.5$ at $z = 2.3$ for a quasar with $E(B - V) = 0.75$. This is $\simeq 1.3$ mag brighter than M^* at these redshifts, where the bulk of the luminosity is produced. A larger survey to fainter K -band limits is required to determine the exact fraction of reddened quasars down to the knee of the intrinsic quasar luminosity function and hence quantify what fraction of the accretion luminosity for the Type 1 AGN-population is generated in an obscured phase.

Our result, that reddened quasars are more common at bright absolute magnitudes, contrasts with observations of intrinsically less luminous AGN-populations, where the obscured fraction shows the opposite trend and decreases with increasing luminosity (Ueda et al. 2003). On the other hand, Assef et al. (2014) have recently studied the space density of the highly obscured population of *WISE*-selected HyLIRGs, which overlap our sample in terms of both luminosity and redshift, but have higher extinctions. They also find that the fraction of obscured luminous AGN is significant at very high luminosities.

Our sample is not large enough to merit fitting a parametric form for the evolution of the reddened quasar LF as a function of redshift. Nevertheless, the differences in the cumulative number counts of unobscured quasars seen from the LEDE and PLE LFs in this redshift range, can help shed light on the kind of evolutionary model that may be appropriate. Starting with the SDSS+BOSS luminosity functions in Fig. 9 and assuming that (i) the extinction

is independent of luminosity and (ii) that every quasar possesses a reddening between $0.5 < E(B - V) < 2.0$ with reddening values drawn randomly according to a flat probability distribution in this range, we can estimate how many reddened quasars we would have observed in our survey area employing the completeness function shown in Fig. 7. These predicted counts, when compared to our observed counts, can then help determine whether the underlying luminosity distribution of reddened quasars, is indeed the same as that of unobscured quasars. Based on the normalisation provided by the BOSS LEDE LF, we predict 15 ± 4 reddened quasars would be detected in the Bright Sample, which is lower than the 21 quasars we have observed. Adopting instead the $E(B - V)$ distribution inferred from SDSS quasars by Hopkins et al. (2004) rather than a flat $E(B - V)$ distribution in the range $0.5 < E(B - V) < 2.0$, results in 0.35 ± 0.59 quasars predicted in our survey. The dramatic difference in the number of objects provides a direct illustration of the need to incorporate near-IR photometric selection in order to identify quasars with reddenings of $E(B - V) \simeq 0.5$ –1.0. Finally, adopting the BOSS PLE LF model instead, which has a brighter break-luminosity (M^*) than the LEDE model, results in a larger space density for the most luminous quasars as evident in Fig. 9. As a consequence, using the normalisation from the PLE LF-evolution model would predict a larger number of reddened quasars in our Bright Sample - 34 ± 4 . Neither model, together with the assumption that the extinction is independent of luminosity, provides a good match to our observed number counts of reddened quasars. The SDSS+BOSS LEDE LF produces too few reddened quasars while the PLE LF produces too many. The results demonstrate that reddened quasars with $-27.0 < M_i < -30.0$ do not possess the same intrinsic [unreddened] LF as unobscured quasars unless the intrinsic luminosity and the $E(B - V)$ distribution are related. Qualitatively, the probability that a quasar possesses a significant $E(B - V)$ must be greater for intrinsically more luminous objects in order for the SDSS+BOSS luminosity distributions to be consistent with our data. The quasar luminosity and reddening are thus not independent. A model in which the probability of a quasar having high $E(B - V)$ increases with increasing luminosity would be viable. However, in the conventional AGN unification model, incorporating a receding torus, the dependence is predicted to take the opposite sign. Alternatively, for an explanation related to some element of the AGN-fueling or life-cycle, individual quasars could experience episodes where both the luminosity and the $E(B - V)$ increase, causing them to migrate brightward in the quasar LF for a period determined by the lifetime of the fueling cycle.

While the number of quasars in our Faint Sample is modest, if we calculate the observed number density of reddened quasars down to $K = 18.9$ (Bright) and 19.3 (Faint) we obtain surface densities of $0.04 \pm 0.01 \text{ deg}^{-2}$ and $0.04 \pm 0.03 \text{ deg}^{-2}$ respectively. The Poisson error associated with the Faint Sample is large but the result provides additional evidence that the LF of the reddened quasar populations continues to increase only slowly down to fainter absolute magnitudes.

Assef et al. (2014) came to the same conclusion using an independently selected sample of more highly obscured AGN from *WISE*. Our sample covers a larger dynamic range in terms of intrinsic quasar luminosity as well as selecting quasars that fall at the lower boundary of their $E(B - V)$ distribution. In combination, the two investigations provide evidence for the existence of a significant population of optically-obscured, hyperluminous quasars with $E(B - V) > 0.5$, with our results probing smaller reddenings and fainter intrinsic luminosities than those in Assef et al. (2014). Quasars with $E(B - V) \gtrsim 1.5$ are not included in our sample as

their observed K -band magnitudes put them below the flux limit of our survey. At the bright-end however, Assef et al. (2014) have confirmed the existence of a population of quasars with such extinctions. The space-densities shown in Fig. 9 therefore represent a lower limit to the numbers of obscured quasars that may be missing from optical surveys.

7 CONCLUSIONS

We have presented a search for heavily dust-obscured luminous quasars at $z > 2$ selected from the new wide-field infrared photometry provided by the UKIDSS Large Area Survey, the ESO VISTA Hemisphere Survey and the *WISE* All Sky Survey. From 48 candidates, we used VLT-SINFONI NIR spectroscopy to confirm 24 new $z > 2$, heavily reddened broad-line quasars with $0.5 < E(B - V) < 1.5$. Three of these new quasars (VHSJ2028–5740, ULASJ2315+0143 and ULASJ0123+1525) have $E(B - V) > 1$ and correspond to the dustiest broad-line Type 1 quasars known. Combining the new quasars with objects presented in B12 & B13, the full sample consists of 38 spectroscopically confirmed, heavily reddened quasars, 36 of which are at $z > 2$. There is no evidence for these near infrared selected reddened quasars having systematically different $H\alpha$ equivalent widths relative to their unobscured counterparts. We present a space density estimate for the reddened quasar population at $z \sim 2 - 3$ enabling detailed comparisons to the space-density of unobscured quasars over the same redshift and luminosity range. In particular, we reach the following conclusions:

- The reddened quasars have very high bolometric luminosities and black-hole masses that are comparable to the brightest unobscured quasars at these redshifts. The median bolometric luminosity of the new sample presented here is $\log_{10}(L_{\text{bol}}/\text{erg s}^{-1}) = 47.1 \pm 0.4$ and the median black-hole mass is $\log_{10}(M_{\text{BH}}/M_{\odot}) = 9.7 \pm 0.4$, consistent with our previous samples of reddened quasars. There is some evidence for the presence of a tail of quasars out to very high bolometric luminosities of $\sim 10^{48}$ erg/s. Around 70 per cent of the reddened quasars have Eddington ratios of $L/L_{\text{Edd}} > 0.1$ confirming the presence of massive black-holes accreting at a high rate. Apart from the high dust extinctions along the line-of-sight, the properties of the reddened quasars appear to be similar to luminous unobscured quasars.

- We compile *WISE* photometry out to $22 \mu\text{m}$ for all our reddened quasars and using a simple power-law fit to the rest-frame $1-4 \mu\text{m}$ SED, we show that the power law indices in the reddened quasars are consistent with those measured for unobscured quasars from the SDSS over the same redshift range and down to the same K -band magnitude limit. The mean power-law index ($\lambda F_{\lambda} \propto \lambda^{\beta_{\text{NIR}}}$) at rest-frame wavelengths of $1-4 \mu\text{m}$ is $\beta_{\text{NIR}} = 0.69 \pm 0.29$ for the reddened quasars compared to 0.50 ± 0.26 for the unobscured quasars. The reddened quasars have slightly steeper power-law indices on average due to the non-negligible extinction at rest-frame wavelengths of $1 - 2 \mu\text{m}$ for some of our reddest objects.

- We use the subset of 25 $22 \mu\text{m}$ -detected reddened quasars to calculate their rest-frame mid infrared $6 \mu\text{m}$ luminosity. We find an average value of $\log_{10}(L_{6\mu\text{m}}/\text{erg s}^{-1}) = 47.1 \pm 0.4$ compared to $\log_{10}(L_{6\mu\text{m}}/\text{erg s}^{-1}) = 46.8 \pm 0.2$ for equivalent SDSS $22 \mu\text{m}$ -detected quasars. The most luminous *WISE* HyLIRG, WISEJ1814+3412 has $\log_{10}(L_{6\mu\text{m}}/\text{erg s}^{-1}) = 47.30 \pm 0.05$ and we find seven of our sample are more luminous at $6 \mu\text{m}$ than WISEJ1814+3412. The $6 \mu\text{m}$ rest-frame luminosities are robust, estimated purely from the observed *WISE* photometry without assumptions regarding the quasar SED or the extinction law, corroborating our conclusion that these reddened quasars constitute some of the most luminous quasars known at these epochs.

orating our conclusion that these reddened quasars constitute some of the most luminous quasars known at these epochs.

- We present the first estimate of the space density of reddened ($0.5 < E(B - V) < 1.5$) quasars at $z \sim 2 - 3$. We find that the most luminous reddened quasars, with de-reddened $M_i < -29$, are at least as numerous at these epochs as unobscured quasars. We also find however that the reddened quasar luminosity function has a much flatter slope and the number density of unobscured quasars, due to the rapidly rising luminosity function, greatly exceeds that of the reddened population by $M_i \sim -27.5$. The slower increase in the number of reddened quasars as a function of decreasing luminosity suggests that as a whole, luminous reddened Type 1 quasars likely do not account for a significant fraction of the total energy liberated by the Type 1 AGN population in an ‘obscured’ phase.

- The observed evolution of the reddened quasar space-density with luminosity is also opposite to that seen in the much less luminous Type 2 AGN samples and to the predictions from the receding torus model, where the obscured fraction is predicted to increase with decreasing luminosity. Our population of reddened quasars therefore probe a very different region of the luminosity-extinction parameter space compared to these Type 2 AGN samples, which have previously been selected through deep, small-area surveys in the X-ray and mid infra-red.

- We test whether different assumptions for the reddened quasar luminosity function, based on the luminosity function of unobscured quasars, are able to reproduce our observations. A model where the luminosity and density are evolving with redshift (LEDE model), and the normalisation is set by the space-density of unobscured quasars, produces too few reddened quasars if the extinction is independent of luminosity. A pure luminosity evolution (PLE) model with a brighter break luminosity reproduces better the observed counts of reddened quasars in the brightest absolute magnitudes in our survey, but in general results in too many reddened quasars being predicted in our survey. Neither model together with the assumption that extinction is independent of luminosity, is able to reproduce the observed number counts of reddened quasars which demonstrates that either reddened quasars do not have the same intrinsic luminosity distribution as unobscured quasars, or that the extinction must depend on luminosity. A more elaborate model, involving an increase in the probability of finding high extinction quasars at high luminosities, would be consistent with the observations. Qualitatively, this behaviour could be related to some element of the AGN fuelling cycle where both the extinction and luminosity increase for a period, causing the quasars to migrate brightward in the luminosity function.

We conclude that our sample of high redshift ($z \sim 2.5$), heavily reddened ($0.5 \lesssim E(B - V) \lesssim 2$), hyperluminous ($L_{\text{bol}} \gtrsim 10^{13} L_{\odot}$) quasars effectively bridge the gap between the optically-luminous, unobscured, quasars known at these redshifts and the much more heavily obscured AGN ($E(B - V) \gtrsim 5$) now emerging from the *WISE* All-Sky Survey. We demonstrate that sensitive near-infrared observations such as those provided by the UKIDSS Large Area Survey (in the northern hemisphere) and the VISTA Hemisphere Survey (in the southern hemisphere), are critical for identifying the population of quasars with intermediate extinctions at high redshift. The space density of such obscured quasars dominates the total quasar counts at very bright luminosities but they are unlikely to account for a significant fraction of the total energy liberated by the luminous, Type 1 AGN population. Reddened quasars likely constitute a brief evolutionary phase in galaxy formation associated with high luminosities and moderate extinctions

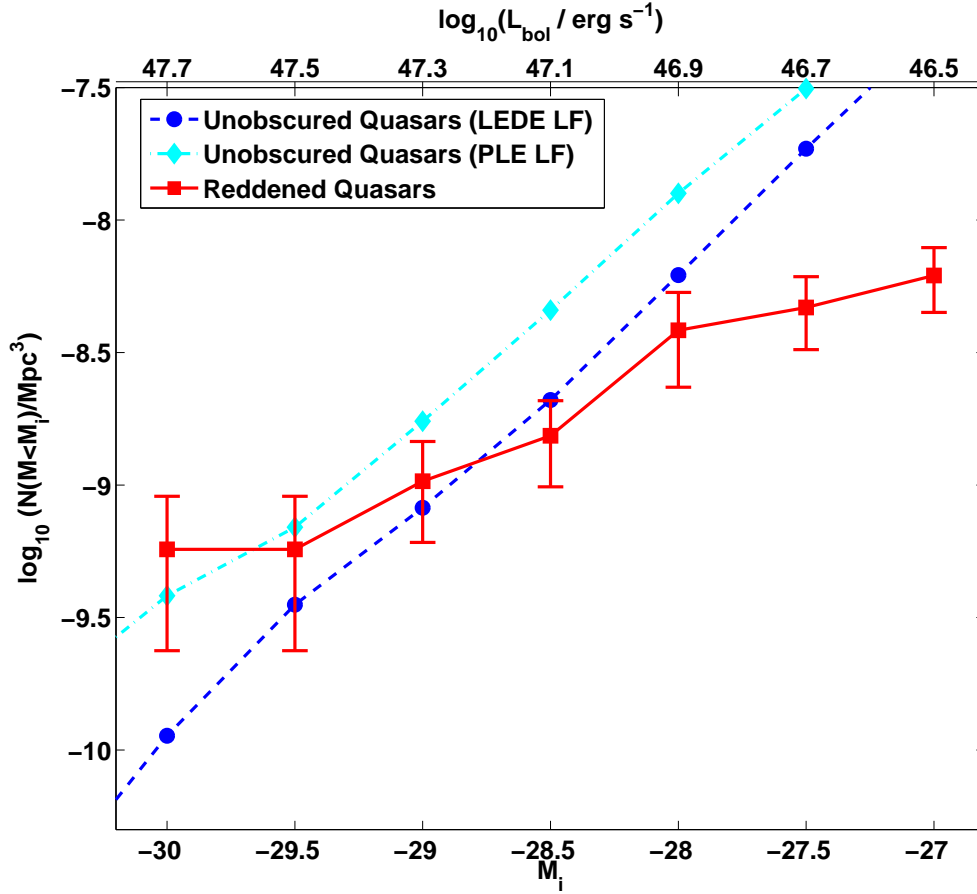


Figure 9. Completeness-corrected, V/V_{max} estimates of the cumulative number density of reddened quasars (red solid) compared to the equivalent cumulative number-densities of unobscured quasars derived over the same redshift and luminosity range assuming the SDSS+BOSS LEDE LF model from Ross et al. (2013) (blue dashed) and the SDSS+BOSS PLE LF from Ross et al. (2013) (cyan dot-dashed). Reddened quasars appear to dominate the counts at high intrinsic luminosities but their number counts flatten off relative to unobscured quasars as we approach more typical quasar luminosities.

towards the quasar line-of-sight. Discriminating between different models for the evolution of these AGN, as they experience changes in their black hole growth rate, L/L_{Edd} , degree of obscuration and outflow properties, will require multi-wavelength investigations of carefully selected sub-samples of objects and is now becoming possible with sensitive NIR integral field units (e.g. SINFONI on the VLT) and ALMA.

ACKNOWLEDGEMENTS

MB is grateful for the assistance provided by the staff at the ESO Paranal Observatory, in particular Jonathan Smoker and John Carter, during the Visitor Mode observations that were conducted for this analysis. Based on observations obtained as part of the VISTA Hemisphere Survey, ESO Program, 179.A-2010 (PI: McMahon) and the ESO Program, 091.A-0341 (PI: Banerji).

REFERENCES

- Alexandroff R., Strauss M. A., Greene J. E., Zakamska N. L., Ross N. P., Brandt W. N., Liu G., Smith P. S., Ge J., Hamann F., Myers A. D., Petitjean P., Schneider D. P., Yesuf H., York D. G., 2013, MNRAS, 435, 3306
- Annis J., et al., 2011, ArXiv e-prints
- Antonucci R., 1993, ArA&A, 31, 473
- Ashby M. L. N., et al., 2013, ApJS, 209, 22
- Assef R. J., Eisenhardt P. R. M., Stern D., Tsai C.-W., Wu J., Wylezalek D., Blain A. W., Bridge C. R., Donoso E., Gonzales A., Griffith R. L., Jarrett T. H., 2014, arXiv:1408.1092
- Assef R. J., Stern D., Kochanek C. S., Blain A. W., Brodwin M., Brown M. J. I., Donoso E., Eisenhardt P. R. M., Jannuzi B. T., Jarrett T. H., Stanford S. A., Tsai C.-W., Wu J., Yan L., 2013, ApJ, 772, 26
- Avni Y., Bahcall J. N., 1980, ApJ, 235, 694
- Baldwin J. A., 1977, ApJ, 214, 679
- Banerji M., Fabian A. C., McMahon R. G., 2014, MNRAS, 439, L51
- Banerji M., McMahon R. G., Hewett P. C., Alaghband-Zadeh S., Gonzalez-Solares E., Venemans B. P., Hawthorn M. J., 2012, MNRAS, 427, 2275
- Banerji M., McMahon R. G., Hewett P. C., Gonzalez-Solares E., Koposov S. E., 2013, MNRAS, 429, L55
- Bongiorno A., et al., 2014, MNRAS, 443, 2077
- Brusa M., et al., 2010, ApJ, 716, 348
- Brusa M., et al., 2014, arXiv:1409.1615

- Civano F., et al., 2012, *ApJS*, 201, 30
- Donley J. L., Koekemoer A. M., Brusa M., Capak P., Cardamone C. N., Civano F., Ilbert O., Impy C. D., Kartaltepe J. S., Miyaji T., Salvato M., Sanders D. B., Trump J. R., Zamorani G., 2012, *ApJ*, 748, 142
- Eddington A. S., 1913, *MNRAS*, 73, 359
- Eisenhardt P. R. M., et al., 2012, *ApJ*, 755, 173
- Fabian A. C., 2012, *ArA&A*, 50, 455
- Francis P. J., Drake C. L., Whiting M. T., Drinkwater M. J., Webster R. L., 2001, *PASA*, 18, 221
- Glikman E., Helfand D. J., White R. L., 2006, *ApJ*, 640, 579
- Glikman E., Helfand D. J., White R. L., Becker R. H., Gregg M. D., Lacy M., 2007, *ApJ*, 667, 673
- Glikman E., Urrutia T., Lacy M., Djorgovski S. G., Mahabal A., Myers A. D., Ross N. P., Petitjean P., Ge J., Schneider D. P., York D. G., 2012, *ApJ*, 757, 51
- González-Solares E. A., Irwin M., McMahon R. G., Hodgkin S., Lewis J. R., Walton N. A., Jarvis M., Marchetti L., Oliver S., Pérez-Fournon I., Siana B., Surace J., Vaccari M., 2011, *MNRAS*, 416, 927
- Greene J. E., Alexandroff R., Strauss M. A., Zakamska N. L., Lang D., Liu G., Patakiwanich P., Hamann F., Ross N. P., Myers A. D., Brandt W. N., York D., Schneider D. P., 2014, *ApJ*, 788, 91
- Greene J. E., Ho L. C., 2005, *ApJ*, 630, 122
- Hao H., Elvis M., Civano F., Lawrence A., 2011, *ApJ*, 733, 108
- Hopkins P. F., Hernquist L., Cox T. J., Kereš D., 2008, *ApJS*, 175, 356
- Hopkins P. F., Strauss M. A., Hall P. B., Richards G. T., Cooper A. S., Schneider D. P., Vanden Berk D. E., Jester S., Brinkmann J., Szokoly G. P., 2004, *AJ*, 128, 1112
- Kaspi S., Maoz D., Netzer H., Peterson B. M., Vestergaard M., Jannuzi B. T., 2005, *ApJ*, 629, 61
- Kaspi S., Smith P. S., Netzer H., Maoz D., Jannuzi B. T., Givon U., 2000, *ApJ*, 533, 631
- LaMassa S. M., et al., 2013, *MNRAS*, 436, 3581
- Lawrence A., et al., 2007, *MNRAS*, 379, 1599
- Maddox N., Hewett P. C., Péroux C., Nestor D. B., Wisotzki L., 2012, *MNRAS*, 424, 2876
- Maddox N., Hewett P. C., Warren S. J., Croom S. M., 2008, *MNRAS*, 386, 1605
- Magain P., Surdej J., Swings J.-P., Borgeest U., Kayser R., 1988, *Nature*, 334, 325
- Martínez-Sansigre A., Rawlings S., Lacy M., Fadda D., Marleau F. R., Simpson C., Willott C. J., Jarvis M. J., 2005, *Nature*, 436, 666
- Matsuoka K., et al., 2013, *ApJ*, 771, 64
- McMahon R. G., Banerji M., Gonzalez E., Kaposov S. E., Bejar V. J., Lodieu N., Rebolo R., the VHS Collaboration 2013, *The Messenger*, 154, 35
- Narayanan D., et al., 2010, *MNRAS*, 407, 1701
- Netzer H., Lira P., Trakhtenbrot B., Shemmer O., Cury I., 2007, *ApJ*, 671, 1256
- Pâris I., et al., 2014, *A&A*, 563, A54
- Pei Y. C., 1992, *ApJ*, 395, 130
- Raimundo S. I., Fabian A. C., Bauer F. E., Alexander D. M., Brandt W. N., Luo B., Vasudevan R. V., Xue Y. Q., 2010, *MNRAS*, 408, 1714
- Richards G. T., et al., 2003, *AJ*, 126, 1131
- Ross N. P., et al., 2013, *ApJ*, 773, 14
- Ross N. P., Hamann F., Zakamska N. L., Richards G. T., Villforth C., Strauss M. A., Greene J. E., Alexandroff R., Brandt W. N., Liu G., Myers A. D., Paris I., Schneider D. P., 2014, *arXiv:1405.1047*
- Sanders D. B., Soifer B. T., Elias J. H., Madore B. F., Matthews K., Neugebauer G., Scoville N. Z., 1988, *ApJ*, 325, 74
- Schmidt M., 1968, *ApJ*, 151, 393
- Schneider D. P., et al., 2007, *AJ*, 134, 102
- Schneider D. P., et al., 2010, *AJ*, 139, 2360
- Shen Y., Richards G. T., Strauss M. A., Hall P. B., Schneider D. P., Snedden S., Bizyaev D., Brewington H., Malanushenko V., Malanushenko E., Oravetz D., Pan K., Simmons A., 2011, *ApJS*, 194, 45
- Stern D., et al., 2012, *ApJ*, 753, 30
- Stern D., et al., 2014, *arXiv:1403.3078*
- Tilton E. M., Shull J. M., 2013, *ApJ*, 774, 67
- Ueda Y., Akiyama M., Ohta K., Miyaji T., 2003, *ApJ*, 598, 886
- Urrutia T., Becker R. H., White R. L., Glikman E., Lacy M., Hodge J., Gregg M. D., 2009, *ApJ*, 698, 1095
- Urrutia T., Lacy M., Becker R. H., 2008, *ApJ*, 674, 80
- Urry C. M., Padovani P., 1995, *PASP*, 107, 803
- Vestergaard M., Peterson B. M., 2006, *ApJ*, 641, 689
- Wang H., Xing F., Zhang K., Wang T., Zhou H., Zhang S., 2013, *ApJL*, 776, L15
- Webster R. L., Francis P. J., Peterson B. A., Drinkwater M. J., Masci F. J., 1995, *Nature*, 375, 469
- Weedman D., Sargsyan L., Leboutteiller V., Houck J., Barry D., 2012, *ApJ*, 761, 184
- White R. L., Helfand D. J., Becker R. H., Gregg M. D., Postman M., Lauer T. R., Oegerle W., 2003, *AJ*, 126, 706
- Whiting M. T., Webster R. L., Francis P. J., 2001, *MNRAS*, 323, 718
- Wright E. L., et al., 2010, *AJ*, 140, 1868
- Wu J., et al., 2012, *ApJ*, 756, 96

APPENDIX A: SPECTRA & SPECTRAL LINE FITS

We present the SINFONI *K*-band spectra for all our spectroscopically confirmed reddened quasars along with the best-fit SED models described in Section 4.1 in Fig. A1. We note that the SED models include a scaling of the H α line to match the observed equivalent width in each quasar. However, no effort has been made to match the velocity widths of the lines as these do not affect the reddening estimates derived from this SED-fitting. The H α line-fits are shown in Fig. A2 in the velocity range ± 10000 km/s. Where double Gaussian fits were possible as described in Section 4.2, the fits show these double Gaussians. For the remaining objects, the fits correspond to a single broad Gaussian. The wavelength dependent noise spectrum is shown as the dashed line in the upper panel while the lower panel shows the fit residuals. The rest-frame full-width-half-maxima for both the single Gaussian and double Gaussian fits, are given in Table A1.

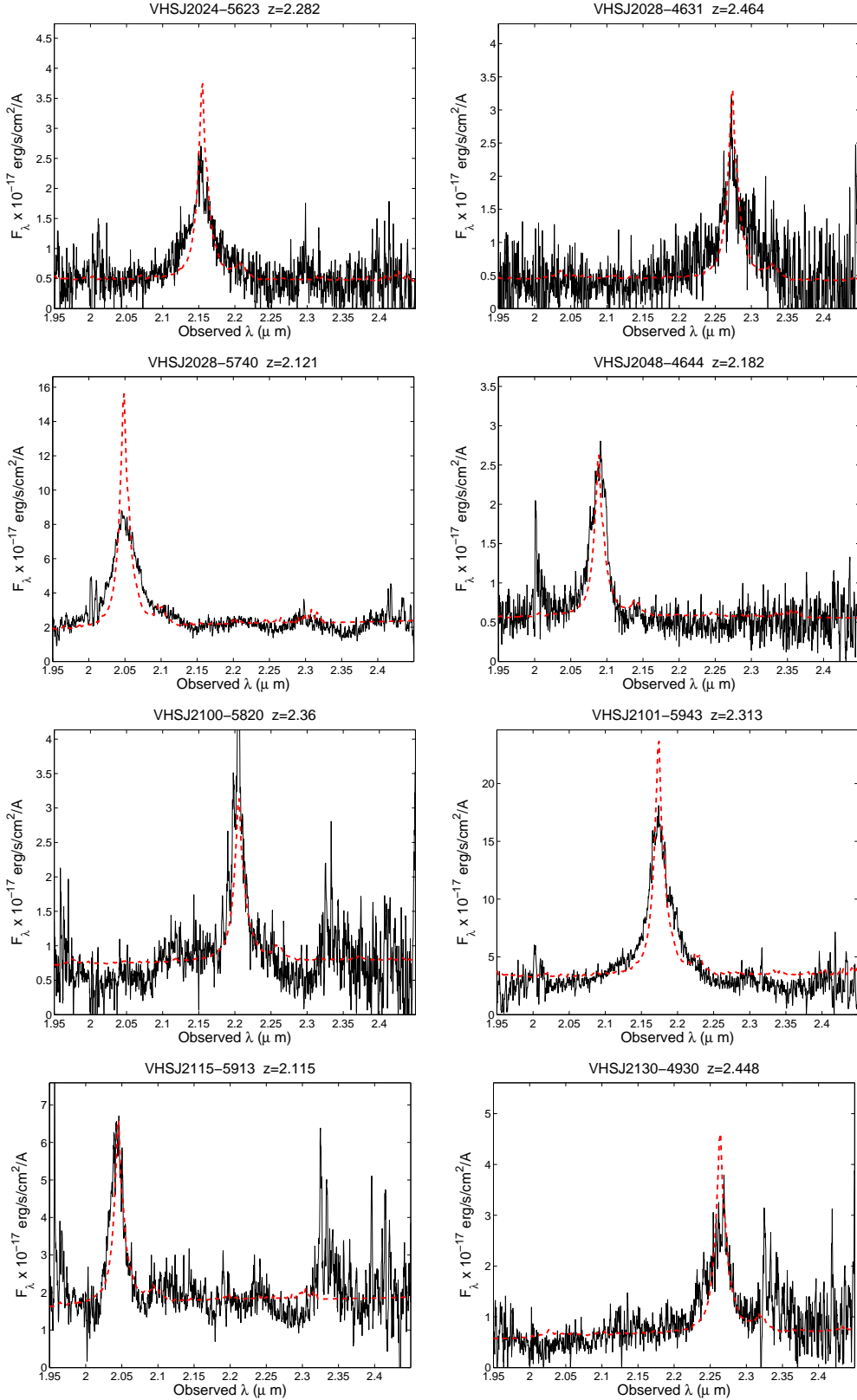


Figure A1. VLT-SINFONI K -band spectra of spectroscopically confirmed reddened quasars (solid line) together with our best-fit SED model (dashed line). Note that the equivalent width of the $H\alpha$ line in the SED model has been adjusted to match the observed equivalent width of each quasar. However, all the SED models assume the same velocity width for the $H\alpha$ line and no effort has been made to match the velocity widths as these do not affect the reddening estimates derived from the SED-fitting.

Table A1. Rest-frame FWHM from both single and double Gaussian fits to the H α line as well as the rest-frame H α equivalent width (EW) for each of our reddened quasars. The double gaussian fit is only considered if the individual components in this Gaussian have FWHM between 1000 and 10000 km/s.

Name	FWHM _{single} /km s ⁻¹	FWHM _{double1} / km s ⁻¹	FWHM _{double2} / km s ⁻¹	Rest-frame H α EW / Å
VHSJ2024-5623	7000	1600	8700	−350
VHSJ2028-4631	4300	–	–	−200
VHSJ2028-5740	6100	–	–	−290
VHSJ2048-4644	4000	–	–	−250
VHSJ2100-5820	3100	–	–	−200
VHSJ2101-5943	5800	3300	9600	−360
VHSJ2115-5913	3000	–	–	−170
VHSJ2130-4930	4400	–	–	−130
VHSJ2141-4816	3900	1100	4600	−210
VHSJ2212-4624	5400	3100	7900	−490
VHSJ2220-5618	3800	1600	5200	−140
VHSJ2227-5203	7300	–	–	−190
VHSJ2235-5750	4900	2100	9000	−260
VHSJ2256-4800	3900	2600	8800	−200
VHSJ2257-4700	4000	2100	5200	−420
VHSJ2306-5447	7900	1500	8600	−500
VHSJ2332-5240	5900	–	–	−300
VHSJ1556-0835	1900	–	–	−230
VHSJ2143-0643	3300	2000	8300	−250
VHSJ2144-0523	3200	2300	9600	−250
VHSJ2109-0026	3500	1900	6900	−320
VHSJ2355-0011	6000	2400	9000	−330
ULASJ0123+1525	3500	1000	4100	−380
ULASJ2315+0143	4700	3000	7000	−270

Figure A1 – continued

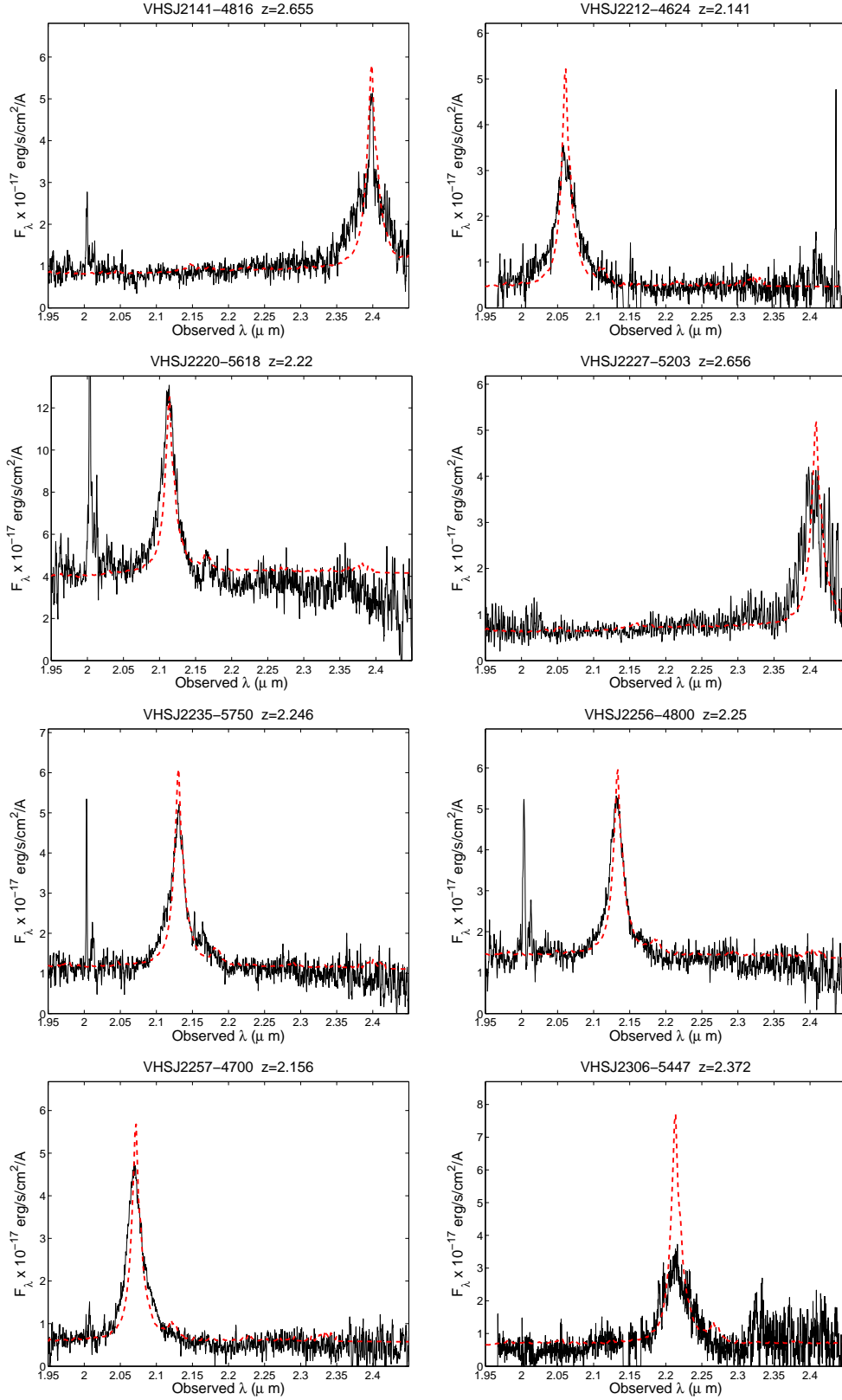
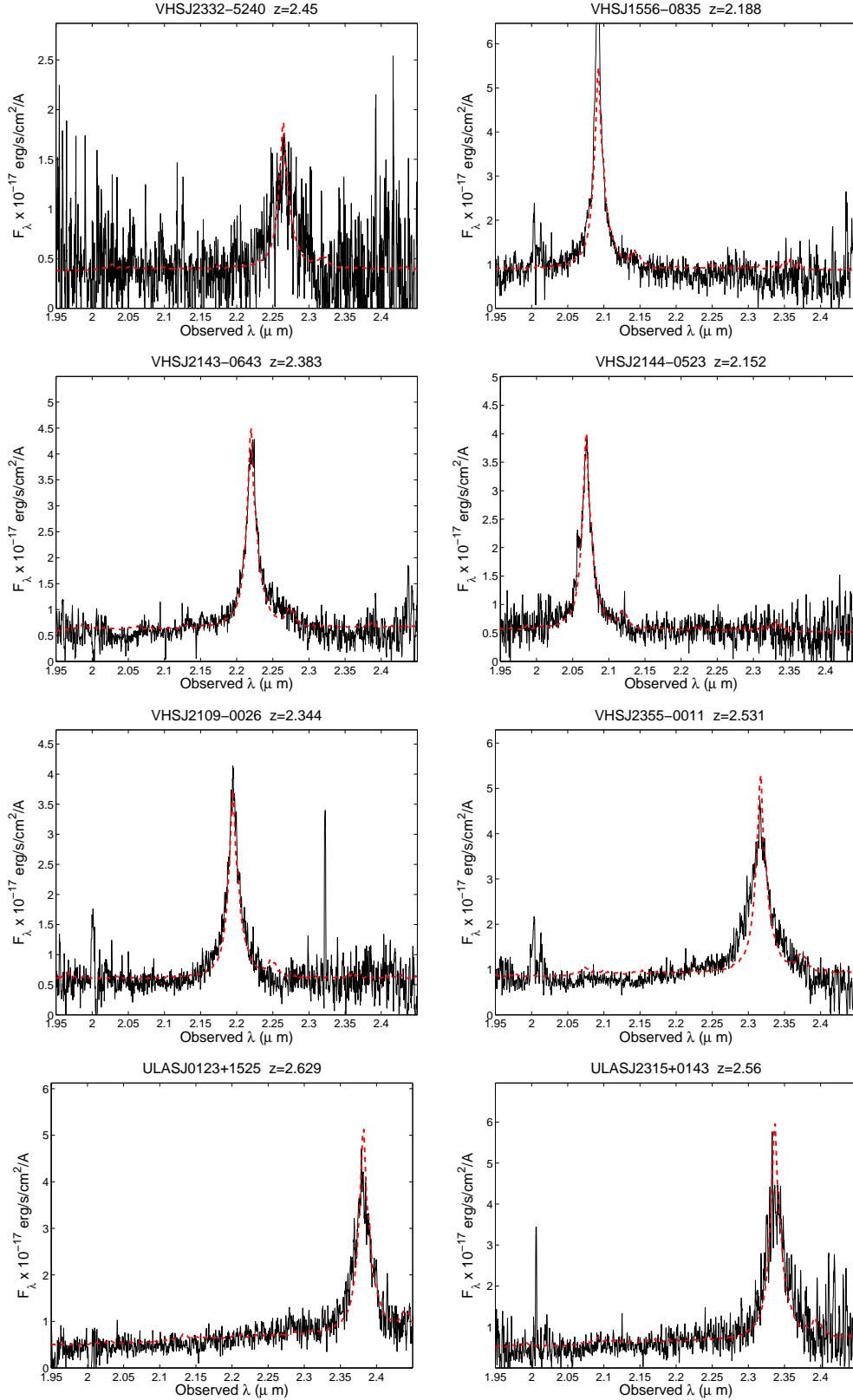


Figure A1 – *continued*

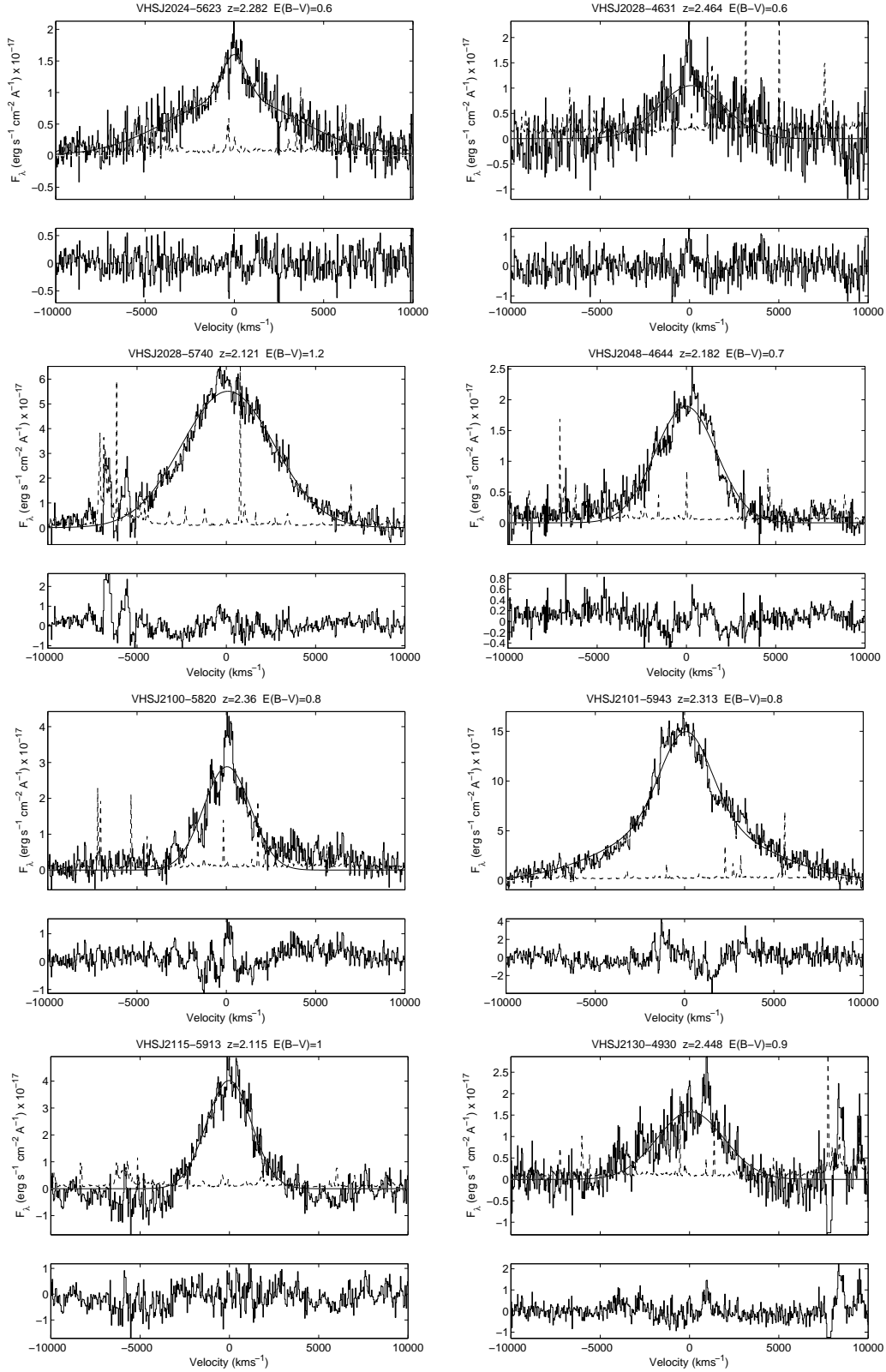


Figure A2. H α line profiles and Gaussian line fits. Bottom panel shows the residuals and the dashed line is the wavelength dependent noise spectrum.

Figure A2 – continued

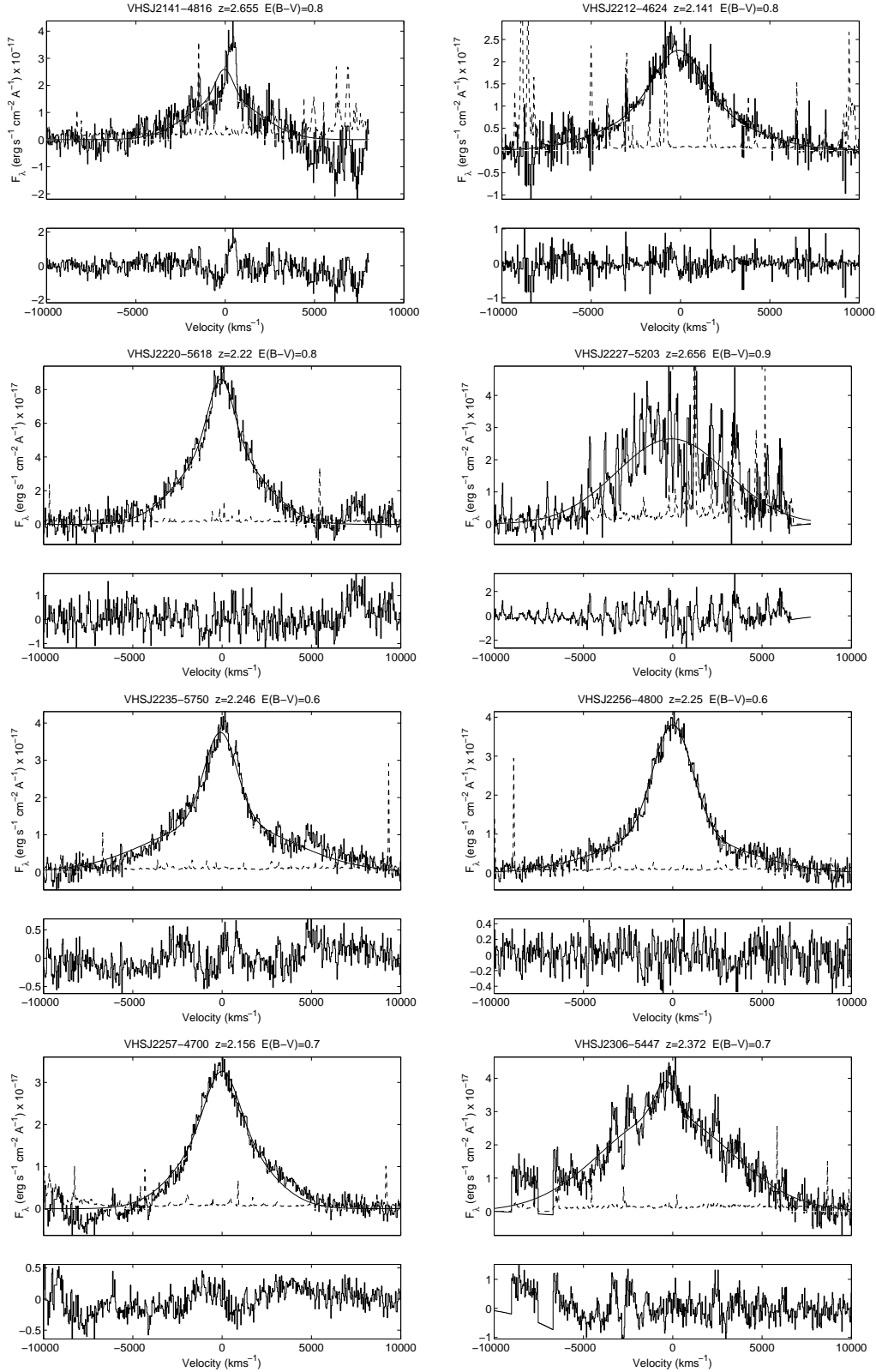


Table B1. K-corrections in the i -band and K -band derived using our quasar SED model from Section 4.1.

Redshift	k_i	k_K
2.00	-1.084	0.506
2.10	-1.078	0.287
2.20	-1.069	0.151
2.30	-1.061	0.118
2.40	-1.064	0.091
2.50	-1.071	0.092
2.60	-1.099	0.131
2.70	-1.153	0.333
2.80	-1.181	0.345
2.90	-1.195	0.321
3.00	-1.196	0.292

APPENDIX B: SED MODEL AND K-CORRECTIONS

Our computations of the quasar bolometric luminosity, absolute magnitude and resulting space density relative to unobscured quasars, implicitly assume the quasar SED model described in Section 4.1. As this SED model is different from several others used in the literature, we provide in Table B1 the i -band and K -band k-corrections for this model over the redshift range of our survey.

Figure A2 – continued

